

Planetary Scale Mapping of Convection Signatures, Thermal Wind Shears and Hadley Circulation in the Upper Jovian Troposphere.

M. de la Torre Juárez[†], B.M. Fisher, G.S. Orton.

[†]M-S 238-600, M-S 169-237, Jet Propulsion Laboratory; Pasadena, CA 91109. U.S.A.

April 19, 2000

Submitted to: *Icarus*

Pages: 43

Figures: 9

Tables: 1

Key words: atmospheres, dynamics, Jupiter, convection, geostrophy, Hadley circulation, infrared observations

Short title: *Mapping convection signatures in Jupiter's upper troposphere*

[†]Send correspondence to: Manuel de la Torre
M-S 238-600; JPL; 4800 Oak Grove Dr.
Pasadena, CA 91109-8099.
e-mail: mtj@cobra.jpl.nasa.gov

Abstract

Convection signatures are inferred in Jupiter's upper troposphere using three tools that are applied to global temperature maps: density maps, three dimensional geostrophy and the mean residual circulation. Each one of the 3 proxies is valid if the large scale transport is controlled by one out of three possible dynamical balances. The balances are the 3 main assumptions behind several theoretical models of the large scale atmospheric dynamics of the major planets. Our goal is to analyze the observations within the framework of each one of these models and, ultimately, relate their predictions with the observations. For one proxy, we introduce a linear formulation of global scale three-dimensional (3D) geostrophy with application to Jupiter, based on the *full* instead of the *primitive* equations of atmospheric flow. Our formulation of 3D geostrophy in a stratified medium includes both the horizontal and vertical projections of the planetary rotation vector. This formulation accounts for the oblateness of the planet, is not singular at the equator, and provides partial information about vertical transport. We also reformulate the hydrostatic approximation for planetary-scale studies. A consequence of the new formulation of hydrostatic balance is the possibility of much smaller wind shears than previously calculated. Scale analysis is used to justify the applicability of linear geostrophic models to Jupiter. The three tools are applied to a set of global temperature maps of the upper Jovian troposphere at four pressure levels, between 100 and 400 mbar, that were obtained from mid-infrared observations made in June, 1996. Maps of the large-scale density distribution at these pressure levels show higher concentration of longitudinal structures along zonal bands at latitudes near 15°N and 15°S . Possible signatures of Hadley cells and their vertical profile are derived from the zonal mean temperatures. We conclude by giving observational criteria that can validate the applicability or not of the theoretical models that inspired our proxies.

1 Introduction

Explaining the ability of planetary flows to display very robust large scale organization remains a challenging problem in planetary sciences. The structure of the Jovian zonal winds is one example of such organization. Several models have attempted to explain these jets. Each model assumes that, on the large scale, Jupiter is dominated by one of several possible dynamical regimes. The most likely regimes are deep convection (*e.g.* Busse 1976), shallow water dynamics (Cho and Polvani 1996), geostrophy (Rhines 1975), and Hadley cell circulations (*e.g.* Williams & Robinson 1973 or, more recently, Condie and Rhines 1994). Simple models of these regimes describe the effects of one of the main forces driving the Jovian atmosphere by assuming that it dominates over the other forces. Each one of the models can explain different aspects of the jets structure and dynamics. The first two approaches motivate our first interpretation of the data, the buoyancy maps, geostrophy will constitute our second. The residual mean circulation will be used as a third approach in order to infer Hadley circulation maps.

Observational data are used here to search for evidence that can elucidate which is the dominant mechanism driving the jets and validate the results and assumptions of the theories. The Voyager 1 and 2, and the Galileo missions added an enormous wealth of information about the Jovian atmosphere. The data revealed very complex dynamics at the cloud top level, and tracking of visible cloud features (*e.g.* Limaye 1986, Vasavada et al. 1998) resulted in quantitative maps of *horizontal* wind velocities at the high spatial resolutions provided by the spacecraft images. However, the retrieval of information at other levels remains a challenge since the clouds act as a thick screen to any observations of the deeper levels. At the same time, the absence of tracers above the clouds hinders the measurement of velocity fields by feature tracking. A breakthrough can be attained at the levels above the clouds to which infrared (IR) observations of thermal emission are sensitive. The temperature fields so derived can be used as a surrogate for horizontal density gradients under the hydrostatic ap-

proximation. Furthermore, Jupiter’s high rotation rate makes geostrophic balance very plausible. Therefore, thermal IR observations offer the best available tool to infer the wind circulation in the upper troposphere and lower stratosphere. If the optically thick cloud level is not a barrier, vertical transport from deeper levels will leave a measurable signature at the heights where IR observations are sensitive. This work presents possible evidence of such signatures.

Voyager IR measurements covering irregular, but dense, grids of Jupiter have been used previously to create zonally averaged temperature profiles from which mean winds were inferred (*e.g.* Pirraglia et al. 1981, Gierasch et al. 1986, who presented zonal average results for 2 pressure levels, and Magalhães et al. 1990) and to analyze the zonal mean residual circulation (Gierasch et al. 1986). The zonal geostrophic winds derived by these authors proved consistent with previous and later results from cloud tracking, thus validating the geostrophic balance assumption. In a more recent review, Gierasch and Conrath 1993 discussed the information gained so far and pointed out the absence of global maps with regular coverage of the full planet. Unlike previous IR data sets, ground based observations provide latitude-longitude maps with constant longitudinal resolution and high signal-to-noise ratio above the clouds.

The other main aspect of this work concerns the formulation of *geostrophy*. Geostrophy is defined as the dynamical balance between the Coriolis forces and the horizontal pressure gradients in a hydrostatically balanced atmosphere. Such conditions are found in very rapidly rotating planets like Jupiter. In geostrophic balance, a velocity field can be caused by horizontal density gradients that induce small deformations of the constant pressure surfaces. These gradients along isobars can be inferred from the temperature gradients measured by IR maps. We discuss here that exact geostrophy balance, as a linear solution to the equation of atmospheric motion, requires hydrostatic balance and is therefore more likely to apply in atmospheric layers that are stably stratified. This is the case of the uppermost tropospheric regions to which our measurements are

sensitive.

The literature presents two approaches to geostrophy. The first results from the linearization of the full three-dimensional equations for models of planetary convection (Chandrasekhar 1961). This approach retains both components (horizontal and radial) of the planetary rotation vector. We will refer to this first approach as ‘global’ or ‘3D’ geostrophy. The second approach stems from the linearization of the primitive equations. It is the most common in atmospheric applications, where only the vertical component of the rotation vector is considered. This method, which we will refer to as the ‘traditional’ approach, is the standard for atmospheric studies, and has been chosen in all the previous studies of geostrophy with IR measurements

The results from the two versions of geostrophic balance differ completely over large scales unless a significant change is introduced into the hydrostatic approximation (de Verdière and Schopp 1994). We discuss this change in section 5.1 and use the term ‘classical’ to refer to the unchanged formulation of the hydrostatic approximation. Note here that ‘traditional’ is used to refer to the geostrophic condition. The most significant result of the new formulation is that it does not diverge at equatorial latitudes. The full 3D equations are at the core of one convective model for the banded flow structure of the major planets (Busse 1976). Its linearized geostrophic version has been discussed in light of non-Oberbeck-Boussinesq models of the major planets (Ingersoll and Pollard 1982) and in gravitational models (*e.g.* Hubbard 1998, and references therein) of Jupiter. It has also been considered for the geodynamo problem (Glatzmaier and Roberts 1997, and references therein), the tidal problem (Miles 1974), equatorial ocean waves (de Verdière and Schopp 1994) and studies of internal convection in the Sun and stars (Brummel *et al.* 1996). Theoretical predictions (*e.g.* Zhang and Schubert 1995, 1996, and references therein) have been made for Jupiter using this 3D approach that have not yet been compared with observations.

The primitive equations set the foundations for atmospheric dynamics and for the

traditional formulation of geostrophy. They are justified using scale analysis of the continuity equation in atmospheric layers where the depth scale is comparable to the density scale (*e.g.* Gill 1982, Pedlosky 1987, and Holton 1992). Shallowness of atmospheric layers suggests much smaller vertical than horizontal velocities. Therefore, the role of the vertical velocities and accelerations can be neglected. However, the neglected terms also involve the horizontal projection of the planetary rotation vector. In the first stages of the present formal development we include the full planetary rotation vector, and, as a consequence, we are required to include the vertical velocity and acceleration. Hence, the resulting 3D geostrophic formulation will include information on vertical transport and waves above the clouds. A discussion on the sufficiency of using only the vertical projection of the rotation vector was presented by Phillips 1965 but questioned by Veronis 1968. A recent work by White & Bromley 1995 has also questioned the validity of the parameterization of the Coriolis terms in the primitive equations used for global circulation models of the Earth's atmosphere. Phillips 1965 justified dropping the vertical velocity and acceleration terms in the momentum equation in order to prevent the violation of angular momentum transfer in the study of shallow atmospheric layers. Veronis 1968 argued that this violation is of the same order of magnitude as other neglected terms. Therefore, shallowness is not a sufficient reason to require use of the primitive equations. Furthermore, Veronis noted that dropping the horizontal component of the planetary rotation is responsible for the singularity in the traditional geostrophic approximation at the equator. The physics near the equator would be ill-represented (*e.g.* as one approaches the equator, Taylor-Proudman columns aligning parallel to the rotation vector must become perpendicular to the local vertical, a result that is prevented in the primitive equations). The necessity of primitive equations could thus not be claimed against the full 3D equations. In a reply to Veronis 1968, Phillips 1968 agreed and gave examples of terrestrial situations where the horizontal component is unimportant and others where it is crucial.

The comparative studies on atmospheric models by Phillips, Veronis, and White & Bromley suggest using geostrophy in Jupiter as the linearization of the full 3D equations for planetary scale diagnostics. Furthermore, the shallow nature of terrestrial atmospheres is not present in Jupiter’s troposphere which extends over many scale heights without any solid boundaries that could set a constraint on the vertical motion. A diagnostic comparison of the observations, using this 3D framework, with theoretical predictions based on this approach has not been tried before in any atmospheric situation (Yano 1994) and is at the essence of this paper.

We restrict this work to the linear balances stemming from the full 3D equations and discuss the resulting hydrostatic approximation and the thermal wind relations. In section 2 the observations and their reduction methods are described. Section 3 presents a scale analysis for Jupiter in order to justify the assumptions used. Section 4 presents density maps as a proxy for buoyancy or convection maps. Section 5 develops and discusses the 3D versions of geostrophy, its effect on the hydrostatic approximation and on the thermal wind, and presents the results obtained after application to our IR measurements. Section 5.2 discusses the error involved in neglecting the nonlinear terms. Section 6 discusses the Hadley circulation. Finally, section 7 discusses the results in light of previous studies and presents our conclusions.

2 Observational method

For application of our 3D geostrophy we have chosen high-quality middle-infrared (mid-IR) data acquired at the NASA Infrared Telescope Facility (IRTF) using the MIRLIN mid-IR camera (Ressler *et al.* 1994) over five nights from June 26 to July 1, 1996. The data consist of images of Jupiter’s disk taken through discrete ($\delta\lambda \sim 0.5 - 1.5\mu\text{m}$) filters at wavelengths of 13.3, 17.2, 17.9, 18.7, 20.8 and 22.8 μm . At the time of the observations, Jupiter was at opposition and had an apparent equatorial diameter of 47 arc-seconds. The telescope diffraction limit, at 18.7 μm , is 1.56 arc-seconds. This

results in a spatial resolution limit of ~ 4700 km, or 3.8 degrees of Jovian longitude, at the sub-earth point.

We chose wavelengths that would sample the Jovian spectrum where it is dominated by the collision-induced opacity of H_2 which is well mixed throughout the region we are sampling. For our temperature retrievals, the Jovian atmospheric radiative properties were modeled by an appropriate combination of H_2 - H_2 and H_2 -He collision-induced absorption (Birnbaum *et al.* 1996). The filter selection provides sensitivity to temperatures between about 100 and 600 mbar. Normalized weighting functions, showing the sensitivity of each wavelength with pressure, are shown in Figure 1. Temperatures were derived for four representative levels: 100, 200, 316, and 400 mbar. The vertical width of the weighting functions define our vertical sensitivity. As can be seen from Figure 1, our range of vertical sensitivity is less than two scale heights, and our retrieval levels are, therefore, not completely independent.

We have not derived the temperatures for pressures greater than 400 mbar, as the influence of a cloud of NH_3 particles (*e.g.* Orton *et al.* 1982; Gierasch *et al.* 1986) could affect these pressures, and we are not yet prepared to separate the temperature and opacity fields from each other for large maps. It is possible that some of our observed 400-mbar structure arises from NH_3 particles. However, the strong similarities between the morphologies of the temperature field derived for the 400-mbar pressure level and those at lower pressures suggests that, for these observations, the temperature field is the dominant factor at 400 mbar.

To retrieve the temperatures from the radiances, we used the nonlinear weighted-Chahine technique (Chahine 1970) for its ease of implementation and robustness. Using this technique, the outgoing radiance spectrum is computed starting with an estimate of the vertical temperature profile. The vertical temperature profile is then perturbed until the outgoing radiance matches the observed radiances at all six wavelengths. A smoothed average of the Voyager 1 radio occultation experiment results (Lindal *et al.*

1981) was used as the initial guess for the vertical temperature profile.

Standard mid-IR reduction techniques were followed to produce the individual images from the raw data. Weather was good enough to provide images with high signal-to-noise ratios. The effects of lower signal-to-noise ratio in the data can be seen in the geostrophic wind shears we derive below, since they rely on spatial derivatives of the data. Typical images were characterized by signal-to-noise ratios of ~ 200 , equivalent to just under 0.1 K in temperature. The worst images we considered have signal-to-noise ratios of about 100, equivalent to just under 0.2 K in temperature. Data with lower signal-to-noise ratios were not considered.

While conditions allowed for good signal-to-noise ratios, the weather was not photometric across the whole acquisition period. Rather than attempting to calibrate through the variable conditions, we scaled all our data to Voyager IRIS belt-zone average radiances. For each image, the Voyager belt and zone average spectra were convolved with our spectral filter functions to create a spectral radiance for each filter. For each image we calculated the ratio of the average of 40° of longitude around the central meridian of the Jovian North Equatorial Belt (NEB), $6\text{--}16^\circ$ N, to the Voyager IRIS spectral average of the same region. This procedure was repeated for the South Tropical Zone (STrZ), $18\text{--}23^\circ$ S. The average of these two ratios produced a calibration scale factor for the image. As expected, our retrieved temperatures are in very good agreement with the He abundance-corrected radio occultation temperature profiles reported by Orton *et al.* 1998. While this method proved convenient and consistent across our data set, it could introduce systematic offsets in the derived temperatures if the NEB/STrZ temperature ratio has changed since the Voyager era, or if Jovian tropospheric temperatures have experienced a systematic shift since the Voyager era.

After calibration, each image was mapped via cylindrical projection onto an even, $1^\circ \times 1^\circ$, grid, with longitudes fixed to the System III rotation rate. Each map is accompanied by a emission angle map. These data, consisting of a radiance and emission

angle pair, for each wavelength, formed the input for the temperature retrievals. The temperature retrievals were done over all (latitude, longitude) grid points whose emission angles were less than 60° . Thus, for each full-disk image set of size wavelengths, four temperature cylindrical projection maps of the visible disk, one at each pressure level, were produced.

Composite global temperature maps were then created by averaging all of the individual maps together. The resulting global composites are shown in Figure 2. The composite maps were formed from data taken as much as 5 days apart. Previous studies of the rotation rates of the longitudinal feature seen in the temperature structure (Deming *et al.* 1989, 1997, Magalhães *et al.*, 1989, 1990, Orton *et al.* 1994) report rotation rates of $\sim 10 \text{ m s}^{-1}$. Such a rotation rate produces a longitudinal smearing of 4300 km ($\sim 3.5^\circ$) over our maximum time difference of five days. This is comparable to our diffraction-limited spatial resolution of $\sim 4700 \text{ km}$. Examining the overlapping longitudinal regions of our data show that actual shifts of discrete, identifiable, features was typically much less than the smearing size of 3.5° . While it is still possible that evolution of the temperature field could have occurred within the period spanned by the data, we did not observe any such evolution above our noise level.

For comparisons to previous work done with zonal mean data, we constructed the zonal mean of our four temperature maps, shown in Figure 3. These zonal means are simply the average value at each latitude, with the error bar the statistical standard deviation of the values at a given latitude. Coverage gaps were excluded from the means.

3 Scale analysis:

Our analysis uses the full 3D equations in spherical coordinates (*e.g.* Holton 1992). These equations are understood as the Reynolds-like equations resulting from a spatial average. The averaging scale is set by the resolution of observations in a similar way as numerical grids set the resolution scale on computational models. The equations are:

- **Equation of state:** $p = p(\rho, T)$ In most of this work we will consider the atmosphere as an inert gas of constant composition and apply: $p = R\rho T/M_r$
- **Continuity** (in absence of internal mass sources or sinks): $\vec{\nabla} \cdot (\rho \vec{v}) = 0$.
Also called *static compressibility* or the *anelastic approximation* (e.g. Ingersoll & Pollard 1982).
- **Momentum** (neglecting viscous effects): ¹ $\frac{D\vec{v}}{Dt} + 2\Omega \vec{k} \wedge \vec{v} = -\frac{1}{\rho} \vec{\nabla} p + \vec{g}$
- **Heat** (for velocities under the speed of sound and if internal heat fluxes are possible) $\left(\frac{\partial}{\partial t} + \vec{v} \cdot \vec{\nabla} \right) \Theta = \frac{J}{C_p}$

In the above equations p is the pressure, ρ is the density, T is temperature, Θ is the potential temperature of a polytropic gas (e.g. Ingersoll and Pollard 1982), R is the gas constant, M_r is the mean molecular weight, \vec{v} is the velocity, Ω is the planetary angular velocity, \vec{g} is the gravity acceleration vector, $J \equiv (p/p_s)^{R/C_p} DQ/Dt$ is the rate of heating per unit mass owing to radiation, conduction and latent heat release, and C_p is the specific heat at constant pressure. Our spatial variables are (x, y, z) with x being the eastward, y the northward, and z the vertical directions. The velocities are (u, v, w) that relate to spherical coordinates $(\vec{e}_\varphi, \vec{e}_\theta, \vec{e}_r)$ by $\vec{v} = u\vec{i} + v\vec{j} + w\vec{e}_r = u\vec{e}_\varphi + v(-\vec{e}_\theta) + w\vec{e}_r$. The horizontal derivatives are along constant log-pressure surfaces. The latitude is $\lambda = \pi/2 - \theta$, where θ is the colatitude. The direction of the rotation axis is defined as $\vec{k} = \vec{e}_r \sin \lambda + \vec{j} \cos \lambda$ and the related axial variable is Z .

¹COMPONENTS OF THE INVISCID MOMENTUM EQUATION:

If gravity is radial and $\vec{v} \equiv (u, v, w)$

$$\frac{\partial u}{\partial t} + \left(w \frac{\partial}{\partial z} + v \frac{\partial}{\partial y} + u \frac{\partial}{\partial x} \right) u - \left(2\Omega + \frac{u}{r \cos \lambda} \right) (v \sin \lambda - w \cos \lambda) = \frac{1}{\rho} \frac{\partial p}{\partial x}$$

$$\frac{\partial v}{\partial t} + \left(w \frac{\partial}{\partial z} + v \frac{\partial}{\partial y} + u \frac{\partial}{\partial x} + \frac{w}{r} \right) v + \left(2\Omega + \frac{u}{r \cos \lambda} \right) u \sin \lambda = \frac{1}{\rho} \frac{\partial p}{\partial y}$$

$$\frac{\partial w}{\partial t} + \left(w \frac{\partial}{\partial z} + v \frac{\partial}{\partial y} + u \frac{\partial}{\partial x} \right) w - \frac{v^2}{r} - \left(2\Omega + \frac{u}{r \cos \lambda} \right) u \cos \lambda = \frac{1}{\rho} \frac{\partial p}{\partial z} - g$$

This system of coupled nonlinear equations is too complex for direct use in diagnostics. Accurate diagnostics would require fully 3-dimensional codes in a spherical geometry. However, significant progress can be achieved by making assumptions which result in simplifications of the equations. Two major basic assumptions, hydrostatic and geostrophic balance, have broad application. They are crucial for IR-data-based diagnostic methods. In order to justify the validity of both assumptions for Jupiter, a scale analysis is needed. Most of the physical values needed for a detailed scale analysis or for a parameterization of the dynamical equations are unknown above the Jovian cloud layers. However, one can estimate upper limits for the different dynamical variables. This will provide a justification for the approximations discussed in this work.

Observations make sub-sonic transport velocities a reasonable assumption above the clouds. We therefore assume that thermodynamic adjustment within each gas parcel occurs faster than dynamical transport. From this and the fact that phase transitions are not observed to play an important role, we expect the perfect gas law to hold as the equation of state and the corresponding heat equation will be assumed to be governed by Newtonian cooling. For the vertical scale that we are considering, observations of the composition make of a constant M_r a reasonable approximation.

Since the diagnostics in section 5 are based on a linear approximation of the momentum equation which is different from the generally accepted, it is necessary to see if the full Coriolis terms are needed when nonlinear terms are neglected. Further, at small velocities, a linear approximation is reasonable. But Jovian winds can reach high velocities that increase the magnitude of the nonlinear corrections. These corrections constrain the validity of a linear approach. To gauge the limits of 3D linear results, we used unrealistically high horizontal velocities to compute upper limits for the nonlinear terms and compare them with the Coriolis term peculiar to our approach.

Table I shows upper limit estimates for the momentum equation. They were obtained considering a three-dimensional sub-sonic velocity. The horizontal components U , V ,

were taken as half the adiabatic speed of sound ($c = \sqrt{\gamma RT_e/M_r} \sim 700 \text{ms}^{-1}$). Using the continuity equation on a predominantly zonal flow, $W \sim U\Delta z/\Delta x \sim 2.5 \text{ms}^{-1}$. These are improbably high values, and thus appropriate for an upper limit to the nonlinear terms. Further, a requirement for using averaged Reynolds equations to analyze the data is that the described fields are smoothly varying in space and time within our measurement resolution. If jumps were present, the limit defining the spatial derivatives would not exist. We chose $\Delta x \sim \Delta y \sim 4700 \text{ km}$, the spatial resolution set by the observations, for the spatial derivatives of our averaged Reynolds equations. The vertical resolution of our weighting functions sets our choice of $\Delta z \sim 25 \text{ km}$. If the velocity changed completely within one grid at these spatial resolution values, it would violate the smoothness required by diagnostics based on a continuum model. Such velocity jumps are not observed. Hence, the chosen combination of low values for the spatial increments together with permitting large velocity jumps artificially inflates the role of the advection terms in our scale analysis. This serves the goal of estimating upper limits to the nonlinear terms in a situation unfavorable to our linear analysis. Table I also includes upper limits for the terms in the heat equation. T_e is the radiative equilibrium temperature assumed constant at constant pressure levels (following *e.g.* Gierasch *et al.* 1986), and $\tau_r \sim 10^8 \text{s}$ (*ibid.*) is the radiative time constant.

The upper limit estimates of Table I make an empirical case for the adequacy of full 3D geostrophically balanced models of Jupiter. Such balance holds when the Rossby number $Ro \equiv |(\vec{v} \cdot \vec{\nabla})\vec{v}|/(2\Omega|\vec{v}|) \sim \Delta U/2\Omega\Delta x \sim 10^{-1}$ is small, as is the case here, and on spatial structures bigger than the Rossby radius of deformation $L_R \equiv N\Delta z/2\Omega \sin \lambda$ (N being the Brunt-Väisälä frequency).

A similar discussion to de Verdière & Schopp's 1994 for the ocean, or White & Bromley's 1995 for the Earth's atmosphere, can be extended to the Jovian values of our table². Remembering that a low Ro reigns in Jupiter and that this implies that

²The most unfavorable scenario occurs if the horizontal velocities on Table I were valid, with a vertical velocity of only about 10 cm s^{-1} . This would affect the comparison of the advection versus the Coriolis term in the zonal

the relative vorticity ξ is $\xi \ll 2\Omega$, we find that even with our unrealistic, unfavorable starting point, the linear Coriolis terms dominate over the nonlinear corrections for the large scale motion.

Finally, our temperature maps are an average of measurements taken over several days. This time scale filters away fast fluctuations and is appropriate for detecting geostrophic effects. The time scale also sets the order of magnitude for the time derivative terms so that, $\partial T/\partial t \sim \Delta T/\Delta t \sim 1/50000 \text{ K s}^{-1}$, $\Delta U/\Delta t \sim \Delta V/\Delta t \sim \Delta W/\Delta t \sim 5 \cdot 10^{-3} \text{ m s}^{-2}$ which are significantly smaller than the dominant terms.

4 Hydrostatic balance, density maps and buoyancy:

This section discusses the effects of pressure deviations from hydrostatic balance that are caused by density changes due to diabatic heating. De Verdière and Schopp 1994 stated that, even in an adiabatic spherical flow, the appropriate hydrostatic approximation differs from the classical form. Their claim highlights that a justification of the hydrostatic approximation in a moving atmosphere using only fluid dynamical principles is not clear. Most frequent proofs require a shallow atmosphere, which is not the case for the major planets. However, the estimates shown in Table I make clear that neither advective, cyclostrophic nor Coriolis accelerations can approach g . In general one can state that if the planetary Froude number $\epsilon \equiv 2U\Omega/g \ll 1$, only the vertical pressure gradient can balance gravity and, hence, hydrostatic balance is a good approximation on Jupiter. This criterion does not require shallowness and depends only on the magnitude of the typical velocity U , the acceleration g , and the rotation frequency Ω . This Froude number allows the introduction of a perturbative approach: $p(x, y, z) \equiv p_h(z) + \epsilon p'(x, y, z) + O(\epsilon^2)$ where $\frac{\partial p_h}{\partial z} = -\rho g$, is the hydrostatic balance solution, $p'/p_h \sim 1$ and the non-dimensional perturbation parameter, the Froude number, is in Jupiter $\epsilon \sim 10^{-3} > \epsilon Ro \gtrsim \epsilon^2$. The ϵ^0

equation. The zonal Coriolis term, fw , becomes $\sim 10^{-3} \text{ m s}^{-2}$, which is one order of magnitude smaller than our upper limit for the full advection term. Yet, zonal advection is given as $(\vec{v} \cdot \vec{\nabla})U \sim U \frac{\partial U}{\partial x} + V \frac{\partial U}{\partial y}$. This nonlinear term compares to both Coriolis terms only if the zonal wind is highly non-zonal $\frac{\partial U}{\partial x}$, or if V is very big. Both possibilities are contradicted by the observations.

solution to the fundamental equations is the one that is in exact hydrostatic balance. Following the Bjerkness-Jeffreys theorem (Houghton 1986), this solution is a barotropic steady state with zero velocity. To the lowest order, the hydrostatic pressure, p_h , depends only on z . The deviations from hydrostatic balance are the pressure anomalies p' . We can also define $T = T_h(z) + \epsilon T'(x, y, z) + O(\epsilon^2)$, where T_h is defined by the basic temperature profile at which hydrostatic balance (no buoyancy) holds. Jupiter's atmosphere is in a diabatic situation where uniform internal heating largely dominates over latitudinal effects due to solar heating (*e.g.* Ingersoll & Porco 1978, Gierasch et al. 1986), we therefore approximate $T_h(z) \equiv \bar{T}_e(z)$, where T_e is the radiative equilibrium temperature and the bar is used to indicate horizontal averaging on a constant pressure surface. Latitudinal temperature changes enter in the higher order T' term. \bar{T}_e is derived from our measurements. In an ideal situation one would like to include the latitudinal dependence of T_e , neglecting it can affect planetary scale conclusions. In this paper we are concerned with comparisons of the observed temperatures with neighboring areas. As a consequence the resulting picture is valid even at global scale, although some caution has to be taken.

The temperatures, retrieved along isobaric surfaces from the IR data, are used to map the deviations from \bar{T}_e . Temperature deviations reflect density deviations. Therefore, the temperature fluctuations in the IR maps can be used to infer density maps. One can take the equation of state for $\rho = \rho(p, T)$ as given by the ideal gas law. Since we are interested in a formulation that includes dynamical states that may be slightly out of thermodynamic equilibrium, a more general result is to take the first approximation of the Taylor series around $\rho_h(z) = \rho(p_h, T_e)$, $\rho(p, T) = \rho_h [1 - \alpha_T(T - T_e) + \kappa(p - p_h) + O(\epsilon^2)]$. In this expression, $\alpha_T = -\frac{1}{\rho} \left(\frac{\partial \rho}{\partial T} \right)_p$ is the coefficient of thermal expansion, and $\kappa = \frac{1}{\rho} \left(\frac{\partial \rho}{\partial p} \right)_T$ is the coefficient of isothermal compressibility. In an ideal gas in equilibrium $\alpha_T = 1/T$, $\kappa = 1/p$. An exact estimate of the density field requires simultaneous measurements of the temperature and the pressure fields. The advantage of IR maps is

that they correspond to constant pressure surfaces up to the measurement resolution. As a consequence, only the thermal expansion term is significant in deriving density maps directly from the temperature maps. When the dynamical region covers many scale heights, variations in potential temperature should be used instead of temperature. Since the observed mixing ratio is approximately constant within these isobars, the potential temperature variations are proportional to temperature variations and an analysis of buoyancy based on temperature is justified. Figures 4a-4d show the normalized density anomalies $\rho'/\rho_h \equiv (\rho - \rho_h)/\rho_h$ to order $O(\epsilon^2)$. These density deviations from the basic state were obtained in the regions between 60°N and 60°S. The gray levels represent arbitrary units. Dark areas correspond to light gas parcels, bright areas correspond to dense gas, and mid-gray levels correspond to neutrally buoyant gas.

Several interpretations of these figures are possible. The first interpretation is that cold areas do not reflect the detection of cold kinetic temperatures at a constant pressure level but, rather, they reflect the increase of atmospheric opacity caused by clouds and hazes forming in upwellings of deeper gas instead of temperatures on isobars. Such an interpretation depends on the independence of the temperature retrieval from interference by clouds. In this interpretation, dense gas parcels are signatures of upwellings from deeper levels while light gas parcels correspond to downwellings.

However, if we can trust that the retrieved temperatures are at a given pressure level, then there is a group of Jovian atmospheric models that predict that the large scale motion is driven by deep convection and can benefit from the buoyancy maps (full 3D overturning models based on Busse 1976; primitive equation models of Hadley circulation such as Condie and Rhines 1994; or without overturning like Williams 1996). Convection models have used the Oberbeck-Boussinesq approximation that defines the buoyancy force $b \equiv -g\rho'$ as proportional to the density anomaly between a fluid parcel and its surroundings. The maps 4a-4d show therefore regions of possible convective transport. The predictions of deep convection models were obtained assuming a basic

density profile that is a linear function of height but which is constant in the continuity equation. Both assumptions have raised much criticism, but there are also results that support the applicability of Oberbeck-Boussinesq models. Addressing the effects of static compressibility, Tritton 1977 and Ingersoll & Pollard 1982 showed that the Oberbeck-Boussinesq equation is still a realistic momentum equation for Jupiter if the temperature is understood as the potential temperature. Authors of deep convection models of Jupiter have repeatedly afterwards mentioned this property (*e.g.* Busse 1983). A second source of criticism, is a constant density profile in the continuity equation (*i.e.* the approximation that $\vec{\nabla} \cdot (\rho \vec{v}) = \rho \vec{\nabla} \cdot \vec{v} = 0$). This assumption remained questionable for Jupiter since the motion occurs over many density scale heights. A simple change into pressure coordinates (*e.g.* Holton 1992, §3.1) can overcome this problem. When the vertical coordinate is p instead of z , the anelastic continuity equation becomes $\vec{\nabla}_p \cdot \vec{v} = 0$, and the vertical velocity is substituted by a new variable $\omega = -\rho_h g w$. The realistic equations in pressure coordinates are thus isomorphic to the momentum and continuity equations of Oberbeck-Boussinesq convection models where the variables T , z , and w were interpreted as Θ , p , and ω . This isomorphism between the continuity and momentum equations of Oberbeck-Boussinesq models and anelastic models, is mentioned again in our Appendix and makes us think that the conclusions of Oberbeck-Boussinesq models may apply on Jupiter.

The general analysis of the role of non-Oberbeck-Boussinesq effects provided by Tritton 1977 advanced that when the Oberbeck-Boussinesq approximation fails, effects like variable viscosity and heat capacity, viscous heating, the effect of the dynamic pressure p' on the buoyancy force and extra effects in the heat equation have the same importance as the non-Oberbeck-Boussinesq terms. Non-Oberbeck-Boussinesq convection studies have only been able to address these effects partially without providing either a very different or as complete a picture as Oberbeck-Boussinesq models (see discussion by Yano 1994 and references therein).

In convection models where the dynamics are driven by buoyancy a colder, denser, parcel of gas will fall, while warming and compressing, and similarly a warmer, lighter, parcel of gas will rise, while cooling and expanding, until each reaches a level where they are surrounded by parcels of the same density. This mechanism involves vertical advection, which is small enough to be compatible with a relative deviation of $\leq g \cdot 10^{-4}$ from hydrostatic balance (as can be seen from Table I). In these models where buoyancy can cause overturning, updrafts would be located in the dark areas of Figures 4a-4d and downdrafts in the brighter areas.

A different type of model used for Jupiter are adiabatic shallow water models (Dowling and Ingersoll 1989, Cho and Polvani 1996). They allow for small deviations from hydrostatic balance which reflect vertical transport. In shallow water models, the thickness of a density surface is computed over a rigid bottom boundary (absent in Jupiter), barotropicity over the layer is assumed, and the continuity equation is imposed only on the horizontal velocities. Barotropicity is a strong assumption. It has been proven (*e.g.* Dritschel & de la Torre Juárez 1996, Dritschel et al. 1999) that the vertical homogeneity of vortical atmospheric flows is broken when their horizontal size L is equal or less than half their height h rescaled as Nh/f ($\sim 100h$ in Jupiter). For example, shallow water models of the biggest vortex, the Great Red Spot, can be justified to less than 10 scale heights. This is only 0.3% of Jupiter's radius. However, these models are also interesting within the range of our measurements. In this approach, density anomalies are small, and overturning is not allowed. Only small vertical velocities are possible, causing a deformation of otherwise horizontal stratification surfaces. Their ultimate signature in IR data would be qualitatively indistinguishable from overturning convection. In these shallow water models, diabatic effects due to radiation, heat release, or conduction do not determine the dynamics, hence the motion will occur within isentropic surfaces. Within the limits of the measurement accuracy, IR observations provide the height difference of the isentropic surfaces from the isobaric surfaces. These surfaces

are bent with respect to the isobars following the temperature deviations shown in the buoyancy maps. Since horizontal motion follows the deformations of these isentropic surfaces and cold gas anomalies reflect a downward deformation of the density surface, an isentropic flow would be deflected and would acquire a negative vertical velocity. On the other hand, warmer areas could arise from an upward deformation as a result of vertical transport of gas from deeper, warmer, levels and horizontal flows can be deflected upwards.

All these interpretations can imply vertical transport. The conclusions from the Oberbeck-Boussinesq, shallow water and motion on isentrope interpretations are in contradiction with the conclusions from the opacity interpretation and with the interpretation stemming from the use of the heat equation addressed in section 6. In the latter two cases cold temperatures can be associated with updrafts and warm temperatures can be associated with downdrafts.

5 Planetary Scale Geostrophic balance:

Another important model of the large scale banded structure of Jupiter is based on the assumption that diabatic effects are not important enough to distort the structure that would be obtained in geostrophic balance (Rhines 1975). One shortcoming of this model is the singularity of traditional geostrophy at the equator. de Verdière & Schopp 1944 discussed the shallow incompressible case that applies to oceans while White & Bromley 1995 did not discussed geostrophy. In this section, compressible (non-Oberbeck-Boussinesq) 3D geostrophy is discussed and it is shown that it shares the main advantages of the shallow incompressible case. As an immediate consequence, the Rhines scenario gains more plausibility.

5.1 The linear approximation:

We now discuss the formulation of linear 3D geostrophy and its differences with the traditional results. This section sets the basis for the discussion of the nonlinear terms in subsection 5.2 and for the thermal wind relations in subsection 5.3 and in the Appendix.

Geostrophic balance is defined as the balance between the Coriolis forces and the pressure gradient in the absence of buoyancy forces:

$$2\Omega\vec{k} \wedge \vec{v}_g = \frac{1}{\epsilon} \left(-\frac{1}{\rho} \vec{\nabla} p + \vec{g} \right) = -\frac{1}{\rho} \vec{\nabla} p_1 + O(\epsilon \cdot Ro, \epsilon^2) \quad (1)$$

It is valid to the order of the neglected advection terms $\sim O(\epsilon \cdot Ro)$. The only ‘peculiar’ aspect in the present work is that \vec{k} is the direction of the rotation axis instead of the local vertical (following, for example, Chandrasekhar 1961; Busse 1976; de Verdière and Schopp 1994). Standard conventions are followed otherwise. The density includes the non-hydrostatic contributions except in the forcing term ³. The total velocity is $\vec{v} \equiv \epsilon \vec{v}_g + O(\epsilon \cdot Ro, \epsilon^2) = \epsilon(u_g, v_g, w_g) + O(\epsilon \cdot Ro, \epsilon^2)$. The second independent perturbation parameter that appears here is Ro . This parameter depends on the amplitude of the solution for \vec{v}_g , and an assessment of its magnitude first requires solving the linear relation (1). From Table I, one can reasonably expect $Ro < 10^{-1}$.

In its traditional form, geostrophic balance also justifies the use of the “classical hydrostatic approximation”: $\frac{\partial p}{\partial z} - \rho g = \epsilon \frac{\partial p_1}{\partial z} = 0$. This equation is a solvability condition, *i.e.* it is necessary in order to allow for an exact solution to expression (1). The gradient of the pressure anomaly in the right side of (1) has to be perpendicular to the rotation vector \vec{k} for the identity to be solvable. In the traditional case \vec{k} is the local vertical (hence the justification of the classical hydrostatic approximation). However, in our case, where \vec{k} is the rotation axis, the solvability condition (*i.e.*

³This is the classical approximation. In a proper sense, making $\frac{\vec{\nabla} p}{\rho} - \vec{g} \equiv \epsilon \frac{\vec{\nabla} p_1}{\rho}$ implies that the pressure anomaly p_1 relates to p' and ρ' from section 4 as $\vec{\nabla} p_1 \equiv \vec{\nabla} p' - \rho' \vec{g}$. Non-hydrostatic buoyancy forces are absent when $\rho = \rho_h + \rho' = \rho_h + O(\epsilon \cdot Ro)$ and hence $p_1 = p'$ but we are keeping a non-buoyant density.

the hydrostatic approximation) becomes a condition on the derivative along that axis:

$$\vec{k} \cdot (-\vec{\nabla} p + \rho \vec{g}) = -\epsilon \frac{\partial p_1}{\partial Z} = O(\epsilon \cdot Ro, \epsilon^2), \text{ or}$$

$$\frac{1}{\rho} \frac{\partial p_1}{\partial Z} = \frac{\sin \lambda}{\rho} \frac{\partial p_1}{\partial z} + \frac{\cos \lambda}{\rho} \frac{\partial p_1}{\partial y} = O(\epsilon \cdot Ro, \epsilon^2) \quad (2)$$

In the traditional formulation, the role of Z is played by z in relation (2), which then reduces to the classical condition $\frac{\partial p_1}{\partial z} = O(\epsilon \cdot Ro, \epsilon^2)$. Therefore, (2) is the correct hydrostatic approximation in a spherical geometry. It has been shown (de Verdière and Schopp 1994) for high Rossby numbers that the nonlinear vorticity terms do not break this condition. A related result has been obtained for the Jovian gravity equipotential surfaces in the deeper levels (Hubbard 1998).

To first order in ϵ , the solution to the linear equation (1) is given by:

$$\vec{v}_g = \frac{1}{2\Omega\rho} (\vec{k} \wedge \vec{\nabla} p_1) = \frac{1}{2\Omega\rho} \left(-\sin \lambda \frac{\partial p_1}{\partial y} + \cos \lambda \frac{\partial p_1}{\partial z}, \sin \lambda \frac{\partial p_1}{\partial x}, -\cos \lambda \frac{\partial p_1}{\partial x} \right) \quad (3)$$

As in the classical geostrophic approximation, this solution can also include any arbitrary function in the direction of \vec{k} . A detailed analysis of this indeterminacy is given in the Appendix, where it is shown that it will not influence the 3D thermal wind relations. In the following sections we will assume that this arbitrary function is smaller than the other neglected terms. The expression for the zonal wind can take two forms. If the hydrostatic approximation is used in the non-classical form (2), the expression for the zonal wind is the traditional result $u_g = -\frac{1}{2\Omega\rho \sin \lambda} \frac{\partial p_1}{\partial y}$. Note, however, that the singularity at the equator is now prevented by the new hydrostatic approximation, which assures that, in geostrophic balance, the latitudinal pressure gradient must be zero at the equator (since $\sin \lambda = 0$). Applying the hydrostatic approximation in its classical formulation leads to $u_g = -\frac{\sin \lambda}{2\Omega\rho} \frac{\partial p_1}{\partial y}$ which differs strongly from the traditional result. The classical hydrostatic approximation would violate the solvability condition (2), and therefore (3) can be a solution only if $\partial p_1 / \partial y = 0$. However its use is defended by White

& Bromley 1995 as causing a smaller error in global scale studies than taking \vec{k} for the local vertical. A discussion of this approach for deriving the thermal wind is given in section 5.3. For both forms of the hydrostatic approximation, the singularity problem of (3) at the equator is absent since the condition $\partial p_1 / \partial y = 0$ always holds there.

Independently of the formulation used for the hydrostatic approximation, several properties become apparent from (3). First, it is straightforward to check that \vec{v}_g fulfills the continuity equation. Therefore, even if the vertical velocity terms had been neglected *a priori*, using the continuity equation on the expression for the horizontal velocities would yield the same vertical velocity as (3). This is an advantage over the traditional approximation where continuity does not hold unless λ is a constant. Second, the meridional and the vertical geostrophic velocities are of the same order of magnitude. This result is consistent with observations at the cloud level, where the meridional velocities are intermittent in time and localized in space (Vasavada et al. 1998). Evidence has been given (*e.g.* Showman and Ingersoll 1998) that such a localization of the vertical velocities is present in the form of smooth upwellings and downwellings. As a consequence, in the present analysis, vertical velocities will not be ruled out *a priori* if meridional velocities are included. Third, a consequence of (2) is that, at equatorial latitudes where $\sin \lambda = 0$, the meridional pressure gradient must be zero, and, therefore, zonal flows are not compatible with a linear geostrophic situation. The fact that nonzero zonal winds are the observed rule at the equatorial clouds could be a signature of either strong ageostrophic effects or a strong decoupling between the atmosphere and the deep interior rotation, which defines the system of reference with respect to which the zonal winds are usually given. This decoupling is not a new nor an infrequent idea. The Galileo probe detected an abrupt change in the vertical gradient of the horizontal velocity at 5 bar depth (Atkinson et al. 1998). One could speculate with this level as being a dynamical analog of the terrestrial solid surface, but, unfortunately, the rotation period of this deeper level is known only at the probe site.

5.2 Higher orders terms:

The geostrophic equations are a linear approximation, both in the traditional and in the 3D model. Their accuracy is limited by the amplitude of the nonlinear terms which, themselves, depend on the solution. Perturbative arguments can be used to estimate the magnitude of the higher order terms in the momentum equation.

Expression (3) for the geostrophic velocity can be used to estimate the advection term. Let us define $\vec{v} \equiv \epsilon(\vec{v}_g + Ro\vec{v}_a)$ (where \vec{v}_a is the ageostrophic contribution to the total velocity), we can write the nonlinear advection term as:

$$(\vec{v} \cdot \vec{\nabla})\vec{v} = \epsilon^2[(\vec{v}_g \cdot \vec{\nabla})\vec{v}_g + Ro(\vec{v}_g \cdot \vec{\nabla})\vec{v}_a + Ro(\vec{v}_a \cdot \vec{\nabla})\vec{v}_g] + O(\epsilon^2 Ro^2, \epsilon^3)$$

From our scale analysis, Ro is $\leq 10^{-1}$. Therefore, the main contribution to advection is given by the geostrophic velocity and is of order ϵ^2 . Using (3) with the measurements in hand, one can now understand the existing evidence of why linear models have been so successful at the scale of the measurement resolution: the dominant horizontal temperature gradients are latitudinal, thus so are the gradients of the pressure anomalies. Therefore the dominant geostrophic velocity component will be zonal. The advection generated by u_g is dominated by $\vec{v}_g \cdot \vec{\nabla} u_g = u_g \frac{\partial u_g}{\partial x} + v_g \frac{\partial u_g}{\partial y} + w_g \frac{\partial u_g}{\partial z}$. Using expression (3) $v_g \sim w_g$, and the small zonal gradients of the measured temperature imply $v_g, w_g \ll u_g$. These results coincide with the estimates based on the heat equation, and continuity. Hence, the dominant zonal advection term goes as $\frac{\partial u_g}{\partial x} \sim \frac{\partial}{\partial x} \left(\frac{\partial T}{\partial y} \right) \ll \frac{\partial T}{\partial y} \sim u_g$. Advection will then be significantly smaller than the upper limits in Table I. This final result supports the assumption already derived that $Ro \ll 1$ for the real geostrophic winds and that, as a result, large scale zonal advection is a higher-order effect than the zonal Coriolis component caused by the vertical velocity.

5.3 *Thermal wind equation:*

In order to evaluate the geostrophic velocity field using (3), independent simultaneous measurements of 3D pressure and density profiles are needed to order ϵ , which is the order of the velocities. Such measurements are not simple to obtain from remote sensing. Geostrophic balance is therefore frequently applied in the form of the thermal wind relations, which are a direct consequence of the linear geostrophic balance condition and the hydrostatic approximation. In the traditional geostrophic approximation, the thermal wind relations are given as a function of temperature. Alternately, the thermal wind relations stemming from the full 3D anelastic equations have not been presented before (for Oberbeck-Boussinesq fluids see Busse 1978; for a homogeneous fluid see de Verdière & Schopp 1994; for a purely zonal flow in Jupiter see Ingersoll and Pollard 1982). Our goal is to formulate the 3D thermal wind relations as a function of temperature only. The full 3D thermal wind equations using the new hydrostatic approximation (2) do not overcome the requirement of independently measuring two thermodynamic quantities (*e.g.* pressure and temperature) and are therefore presented in the Appendix. Although they are consistent with the order of our perturbation analysis, one needs one extra approximation to make some progress. This assumption involves using the classical hydrostatic approximation.

The classical derivation process of the thermal wind relations are applied to (3) (following Holton 1992, pp. 74-75), using the classical hydrostatic approximation $\frac{\partial p_1}{\partial z} = 0$ (accurate only to order ϵ^0): The partial derivatives along the horizontal are taken in directions perpendicular to the pressure gradient (i.e. $\frac{\partial p_1}{\partial x} = \frac{\partial p}{\partial x}$ and $\frac{\partial p_1}{\partial y} = \frac{\partial p}{\partial y}$). Differentiating relation (3) with respect to pressure and multiplying the result by pressure yields:

$$\begin{cases} \frac{\partial u_g}{\partial z^*} &= -\frac{R \sin \lambda}{2\Omega M_r} \left(\frac{\partial T}{\partial y} \right)_p \\ \frac{\partial v_g}{\partial z^*} &= \frac{R \sin \lambda}{2\Omega M_r} \left(\frac{\partial T}{\partial x} \right)_p \\ \frac{\partial w_g}{\partial z^*} &= -\frac{R \cos \lambda}{2\Omega M_r} \left(\frac{\partial T}{\partial x} \right)_p. \end{cases} \quad (4)$$

Where $z = Hz^* = -H \ln(p/p_0)$, with $H = RT_h/g$ being the pressure scale-height. The reason why the hydrostatic approximation enters to order ϵ^0 is better seen using the classical derivation in terms of the geopotential Φ , where $\frac{\partial \Phi}{\partial p} = -\frac{1}{\rho} = -\frac{RT}{M_r p}$. In terms of Φ , the geostrophic velocities are given as $u_g \sim -\frac{\partial \Phi}{\partial y}$ and $v_g \sim \frac{\partial \Phi}{\partial x}$ where the proportionality factor is $1/f \equiv 1/2\Omega \sin \lambda$ in the traditional case, and either $\sin \lambda/2\Omega$ or $\cos \lambda/2\Omega$ in our new approach. Next, the following permutations are applied on the horizontal derivatives:

$$\frac{\partial u_g}{\partial z^*} = -p \frac{\partial u_g}{\partial p} \sim p \frac{\partial}{\partial p} \left(\frac{\partial \Phi}{\partial y} \right)_p = p \frac{\partial}{\partial y} \left(\frac{\partial \Phi}{\partial p} \right) = -p \frac{\partial}{\partial y} \left(\frac{1}{\rho} \right)_p$$

and

$$\frac{\partial v_g}{\partial z^*} = -p \frac{\partial v_g}{\partial p} \sim -p \frac{\partial}{\partial p} \left(\frac{\partial \Phi}{\partial x} \right)_p = -p \frac{\partial}{\partial x} \left(\frac{\partial \Phi}{\partial p} \right) = p \frac{\partial}{\partial x} \left(\frac{1}{\rho} \right)_p$$

(w_g follows a similar procedure to v_g .) The previous derivative permutations require that f remains constant and that $\partial p/\partial x = \partial p/\partial y = 0$. The first condition is reasonable when regions of small horizontal extent are described. The second condition is compatible with (2) only if $\partial p/\partial z = \partial p/\partial y = 0$, which was shown in section (4) to be justifiable only to order ϵ^0 . Expression A3 in the Appendix describes the result obtained when terms ϵ^1 are kept during the derivation giving rise to horizontal pressure derivative terms. Expressions (4) provide the vertical derivatives of the vertical velocity allowing a direct application to observational data and a comparison with previous results (*e.g.* Gierasch *et al.* 1986).

As in section 5.1, a connection can be made with the traditional result if (2) is used in (3) to evaluate the geostrophic wind \vec{v}_g to order ϵ^1 . The traditional identity $\frac{\partial u_g}{\partial z^*} = -\frac{R}{2\Omega \sin \lambda M_r} \left(\frac{\partial T}{\partial y} \right)_p$ is recovered. This expression is of higher order of approximation than

the zonal component in (4) because the hydrostatic approximation enters here at order ϵ^1 in (3), although it remains of order ϵ^0 in the step that allows the permutation of the derivatives. Despite the similarity with the traditional result, the singularity at the equator remains absent as discussed in section 5.1. This last condition holds in our measurements within the error bars. Some deviations may arise from local effects that break geostrophy, and they cannot be excluded.

Figures 5a-5d, 6a-6d, 7a-7d and 8a-8d show the results of applying (4) to our data. In Figures 5a-5d, the more familiar result of the zonally averaged thermal wind is presented. The results with the classical hydrostatic approximation are presented as closed circles. Applying the new approximation (2) in (3) leads to the same formula as in Gierasch *et al.* 1986 and is shown as open squares. The classical hydrostatic approximation gives rise to much lower values, implying larger vertical depth scales for decay than reported by Gierasch *et al.* 1986. Banfield *et al.* 1996, in an analysis of comet Shoemaker-Levy 9 impact debris, also favored larger vertical scales, and thus smaller wind shears. However, the Banfield results average over a considerable vertical range well into Jupiter's stratosphere while we are confined to the upper troposphere. It is difficult to reconcile these different measurements, particularly given that the results from the Galileo probe (Atkinson *et al.* 1998) show considerable variability in the wind shears with height.

Figures 6 - 8 present the maps for each of the three thermal wind components. For the sake of consistency with the ϵ^0 level of approximation needed to obtain (4) we used the classical hydrostatic approximation on Figures 6a-6d. We are interested in obtaining qualitative information about the sign of the vertical derivative which does not change if either hydrostatic approximation is used. Figures 7a-7d and, more in particular, 8a-8d present the results where our diagnostic method differs substantially from any previous work. All of the figures use the same scaling to facilitate the comparison of relative amplitudes. Banded structures are apparent in the zonal and the vertical

winds at most latitudes. Meridional winds appear rather constant with height. Vertical gradients of the vertical wind reflect the existence of updrafts and downdrafts. In order to determine the sign of the vertical motion, one needs to integrate the thermal wind. This requires knowledge of the wind map at a pressure level to which IR is sensitive, but this is not available. One could assume the cloud-derived zonal wind speeds for the basis of the integration of the zonal component of the thermal wind. However, the large vertical gradients in the wind field at the Galileo probe site (Atkinson *et al.* 1998) call the validity of this assumption into question. Some qualitative information on the sign is gained by comparing with the density maps of Figures 4a-4d that show where buoyancy favors each sign of vertical transport.

6 Heat equation: residual vertical transport:

In this section, the zonal mean of the heat equation is used to diagnose the residual circulation across different latitudes and at different heights following the same approach as Gierasch et al. 1986. If we take the transformed Eulerian mean equations (Holton 1992), the heat equation takes the form

$$\langle w \rangle^* \frac{d\Theta}{dz^*} = \frac{T_e - \langle T \rangle}{\tau_r}$$

which can be addressed with our data. Where the residual vertical velocity is defined on an ideal gas as $\langle w \rangle^* \equiv \langle w \rangle + \frac{R}{H} \frac{\partial}{\partial y} (v' T N^{-2})$. The brackets represent zonally averaged variables, and the total meridional velocity is $v \equiv \langle v \rangle + v'$. The residual vertical velocity represents the part of the mean vertical velocity whose contribution to adiabatic temperature change is not canceled by the eddy heat flux divergence. If eddy heat transport is very small, the residual vertical velocity is the zonal mean of the vertical velocity. Hadley circulation models that have been advanced for the Jovian troposphere (Condie and Rhines 1994) thus benefit from such zonal averages. The results presented below map the possible signatures of Jovian Hadley cells.

From radio occultation data (Lindal *et al.* 1981) and direct measurement (Seiff *et al.* 1998), the vertical gradient of the potential temperature can be assumed to be nearly a constant in the upper troposphere. Using the sign of this gradient and $\langle T \rangle$ from our data, zonal averages of $\langle w \rangle^*$ were determined and are shown for different heights in Figures 9a-9d. We have chosen a T_e independent of latitude, defined as the mean temperature of each pressure level, following the arguments of Gierasch *et al.* 1986. Inclusion of latitude dependence in T_e would be desirable to examine global scale phenomena. We have not done it for two reasons. First, our temperature maps exclude the polar regions leaving a gap in our coverage, although polar tropospheric temperatures are not expected to be very different from the rest of the planet (Ingersoll *et al.* 1976). Secondly, it is unclear what would constitute a good quantitative model for the latitudinal dependence of T_e and whether such a model would introduce more errors than simply assuming a constant T_e . Conrath *et al.* 1990 concluded that the annual mean value of T_e is only weakly dependent on latitude at all pressure levels. Thus any latitude dependence would be driven by shorter-time scale phenomena such as seasonal changes in solar insolation, whose effects on T_e are poorly understood. However, a qualitative discussion is still possible. Our temperature maps exhibit a North-South asymmetry in their higher latitude mean temperatures which is likely attributable to such seasonal effects. If the observed temperature asymmetry exists with similar latitude structure in T_e , then North-South asymmetries in the residual vertical transports would be reduced. The sign of the potential temperature gradient implies that, in the zonal mean and within our measurement resolution, cold latitudes can correspond to updrafts while warm latitudes correspond to downdrafts. This interpretation is due to the fact that horizontal heat advection is not included. The heat transport required to balance horizontal temperature gradients can occur only along vertical gas columns. The resulting conclusion would be that the transport occurs with an average of the vertical velocity which is opposite to the buoyancy arguments.

Several effects are discernible in Figures 9a-9d. First, a North-South hemispheric asymmetry appears to influence the vertical velocities pole-ward of about $\pm 30^\circ$. This asymmetry is consistent with a seasonal effect: The data were taken during winter in the northern hemisphere. Second, an inversion of the vertical velocity appears to take place between 100 and 400 mbar at the northern and southern limits of our coverage. Third, in the deeper levels, the role of vertical transport decays while moving away from the equator. Above 200 mbar, higher latitudes show the larger role of the vertical transport. The results at 316 and 400 mbar show downwelling in the North limit and upwelling in the South which could be a signature of pole-to-pole circulation. Finally, the results suggest that Jupiter may have at least five Hadley cells.

7 Summary and conclusions:

This work incorporates new theoretical and observational results. On the theoretical side, linear geostrophy and the hydrostatic approximation as derived from the full 3D equations for atmospheric flow have been applied for the first time on diagnostics of Jupiter's upper troposphere. The development of a 3D geostrophic formulation for atmospheric diagnostics has resulted in a new set of thermal wind relations. They have been presented in geometric coordinates (and in isobaric form in the Appendix). The connections between the traditional and the global scale formulation have been discussed. Previous results from 3D geostrophy for homogeneous flows have been compared and we have shown in the Appendix that their conclusions can be extended to describe stratified fluid layers. The implications of planetary scale geostrophy on the hydrostatic approximation, thermal wind relations and the non-geostrophic nature of equatorial zonal flows have also been established. In the hydrostatic approximation, a cylindrical symmetry is introduced by relation (2). Another result is that vertical wind shears may be several times smaller than previously thought, depending on the latitude. 3D geostrophy has also provided information on the vertical derivatives of

the three components of the geostrophic wind. This may be useful to infer vertical transport.

On the observational side, three proxies have been used for inferring low-noise regularly gridded maps of vertical transport in the upper Jovian troposphere using ground-based infrared observations. The proxies have been used to obtain planetary scale maps of buoyancy, vertical wind shears, and residual mean circulation. The three proxies used put forward diverse predictions. Some of these are consistent with one another, and some are not. Since the validity of each proxy depends on the dynamical regime that controls the temperature profiles, establishing the validity of each proxy will help to understand the dynamical state of Jupiter at the depth of our observations.

All three proxies imply a large amount of zonal organization. They also show two relatively warm bands centered at 15°N and 15°S that display considerable longitudinal structure, the most prominent of which is the cold Great Red Spot. This and smaller elliptically shaped features have sizes that are several times the Rossby radius of deformation which indicates that geostrophy plays an important role in their dynamics. In general, the maps show little variability with height indicating a high degree of barotropicity (this is not always expected *e.g.* Dritschel et al. 1999 and Dritschel & de la Torre Juárez 1996). In the zonal mean, however, the changes of sign of the zonally averaged vertical wind in Figures 9a-9d imply some baroclinicity at higher latitudes.

Apart from the similarities, there are several differences in the interpretation of the temperature maps that depend on which proxy we choose. These differences are worth mentioning, since the validation of one rather than another will define what are the structures and principles controlling the Jovian winds at these heights. The first difference between the proxies is in the interpretation of the vertical motion associated with the longitudinal structure. The structures observed in the density maps along a given latitude reflect deformations of isobaric surfaces and do not necessarily imply vertical motion. The nonzero values of $\partial w / \partial z^*$ resulting from the geostrophic method

do, however, imply vertical transport. If the usual assumption is taken that the vertical wind derivatives are constant from a level of zero velocity, the vertical gradient of w is proportional to w itself. The longitudinal structures in the latitude bands around 15°N and 15°S represent overturning cells then in the 3D geostrophic interpretation. If overturning really occurs here as predicted by the geostrophic approach, one would expect a significant amount of deeper material being upwelled and subducted more frequently in these two bands than at other latitudes. The observed structures in both, the geostrophy and buoyancy based proxies, would be consistent with a higher standard deviation of the observed concentration of volatiles on these two bands. The third proxy is based on zonal means, and thus it cannot be used for comparison because the averaging procedure masks any longitudinal information.

A second difference is on the location of vertical motion implied by the first two proxies. From (4), an intensification of geostrophic vertical transport should occur where the longitudinal temperature gradients increase and should decay where this gradient approaches zero in order to change its sign when the sign of the gradient changes. Conversely the buoyancy criterion locates the updrafts and downdrafts at the longitudes with local temperature maxima and minima, where the horizontal temperature gradients are close to zero and with symmetric signs of the vertical velocity around these maxima and minima. As a consequence, both dynamical regimes predict different locations of the updrafts and downdrafts.

The third difference is in the picture obtained from the residual mean circulation. Under the restrictions discussed in section 6, the residual mean circulation shows the signatures of the Jovian Hadley cells. In Figures 9 the equatorial latitudes show a constant vertical motion while the higher latitudes show a change of sign with height. This change of sign is consistent with an inversion of the high latitude dynamics within the range of heights observed. Such an inversion is not present in the other two proxies.

A fourth difference is that the direction of vertical transport inferred from the heat

equation for the residual mean circulation, under the assumption of Newtonian cooling, is the opposite to that obtained in a dynamical regime driven by buoyancy. The residual mean circulation appears most consistent with indirect inferences about upwelling and downwelling regions based on the condensate mixing ratios derived, for example, by Voyager IRIS remote sensing data (Gierasch et al. 1986). Cold latitudes correlate well with areas of increased cloud albedo and the warm latitudes correlate with lower cloud albedo. The common interpretation is that regions of high cloud albedo are caused by upwellings that transport condensates from deeper levels increasing the cloudiness and humidity at cold latitudes. In contrast, a dynamical regime driven by buoyancy would imply that warm areas are upwelling and cold parcels of gas are heavier and therefore downwelling. We cannot rule out the proxy which relies on buoyancy for several reasons. First, our interpretations of condensate mixing ratios are based on the assumption that local effects dominate their latitudinal profile. However, the more complete observational knowledge associated with the Earth's transport mechanisms between the upper troposphere and the lower stratosphere shows a complex situation where nonlocal dynamics can outweigh local effects in shaping the planetary scale circulation (Holton et al. 1995). Second, there may be systematic effects involved in the comparison between the depths where we are measuring the temperatures and the depths of the cloud tops. Most of what we know of Jovian dynamics or evidence of transport is based on measurements of tracer features at the cloud-top level. Our IR measurements are sensitive to layers well above, including the transition from the troposphere to the lower stratosphere. This may lead to some phenomena specific to such transition regions. One of them is that a combination of nonlocal transport and a mechanism similar to the freeze-drying of water vapor observed near the convective updrafts at the Earth's tropopause may be also happening in Jupiter. This could cause a lower ammonia mixing ratio located right on the buoyant updrafts. A different possibility would be an inversion of the signs of the vertical velocity and of the horizontal density and temperature gradients. They

are expected between masses of gas above and below regions of strong cyclonic or anticyclonic vorticity (Pedlosky 1987), for example the horizontal temperature gradients reported near the Earth's tropopause (*e.g.* Hoskins et al. 1985, Holton et al. 1995). Such an inversion would be consistent with a regime driven by buoyancy and cannot be excluded in Jupiter with the present observational evidence. It could be responsible for different dynamical regimes at the cloud level and at our observational level (cold areas on top of deeper warm areas). If this inversion were happening in Jupiter, the estimates of zonally averaged ammonia abundances (Gierasch et al. 1986) would need another interpretation. The traditional picture is that higher ammonia concentrations are a manifestation of updrafts carrying material from deeper levels. Such convective overshooting would be accompanied with transport of deeper warmer gas to higher levels and should therefore correlate with a higher temperature than the gas at a similar height, which is not the case. If the inversion is happening, the anticorrelation of ammonia with the buoyancy force, would be reflecting a selective overshooting. The study of transport of lagrangian tracers has shown that particles denser than the surrounding fluid display some sort of 'inertial diffusion' (Crisanti et al. 1990): A passive tracer that is heavier than the fluid with which it moves, carries higher inertia. Once a heavier particle has started motion, it requires a higher drag in order to be stopped and this is the cause for 'inertial diffusion'. Ammonia's higher molecular weight could be causing a possible convective overshooting to higher levels than the surrounding hydrogen. This would open the possibility of ammonia being more abundant in areas where a colder gas, mostly hydrogen, has inverted its vertical velocity and is downwelling. The ultimate arbiter between these competing hypotheses, of course, would be reliable measurements of vertical winds in different regions of Jupiter, but these are unlikely to be available for some time. The absence of visible tracers at these levels above the clouds make in situ measurements the only candidates to solve these puzzles.

APPENDIX: FULL THERMAL WIND RELATIONS.

In this Appendix, we present the thermal wind equations obtained when using the 3D geostrophic condition and the new hydrostatic approximation. This produces a set of equations that are of the same order of approximation as the geostrophic velocity and in which the indeterminacy in the geostrophic velocity does not play a role.

The 3D thermal wind relations are obtained from the vorticity equation after dropping the nonlinear terms. We first rewrite the full momentum equation as

$$\frac{D(\rho\vec{v})}{Dt} + 2\vec{\Omega} \wedge (\rho\vec{v}) = -\vec{\nabla}p + \rho\vec{g}.$$

After dropping the nonlinear terms and the time derivative (*i.e.* using the geostrophic balance condition), we take the curl which, after using some vector identities (*e.g.* Holton 1992) and the anelasticity condition, leads to:

$$-\epsilon(2\vec{\Omega} \cdot \vec{\nabla})(\rho\vec{v}_g) = \vec{\nabla}\rho \wedge \vec{g}. \quad (\text{A1})$$

where the ageostrophic velocity has been neglected. This expression is the 3D vector form of the thermal wind (we are still keeping the full planetary vorticity and, hence, we cannot drop the vertical velocity terms yet), which holds to order $O(\epsilon Ro)$. We note at this point that the indeterminacy in the geostrophic velocity does not change this expression (A1). The reason is that v_g as was given in (3) is non-divergent. As a consequence, if an indeterminacy $A(x, y, z)$ in the direction \vec{k} is allowed, the continuity equation requires that $0 = \vec{\nabla}(\epsilon\rho\vec{v}_g + \rho A(x, y, z)\vec{k}) = \partial\rho A(x, y, z)/\partial Z$. That is, the indetermination does not contribute to the derivative along the rotation axis. Since the thermal wind involves the derivative along the rotation axis, allowing for a nonzero $A(x, y, z)$ may change the geostrophic velocity, but will not affect the thermal wind relations.

Using the no-buoyancy assumption from (1) ($-\vec{\nabla}p + \rho\vec{g} = -\epsilon\vec{\nabla}p_1 + O(\epsilon^2)$), one has:

$$\vec{\nabla}\rho \wedge \vec{g} = \frac{\vec{\nabla}\rho}{\rho} \wedge (\vec{\nabla}p - \epsilon\vec{\nabla}p_1) = \rho\vec{\nabla}\left(\frac{1}{\rho}\right) \wedge (-\vec{\nabla}p + \epsilon\vec{\nabla}p_1).$$

The dominant contribution is hence given by the traditional baroclinic term $\vec{B} \equiv -\vec{\nabla} \left(\frac{1}{\rho} \right) \wedge \vec{\nabla} p$, and the rest will be neglected. IR measurements provide temperature information as a function of pressure. It is therefore desirable to work with the baroclinic term using T and p as the variables. In an ideal gas this yields: $\vec{B} \equiv -\vec{\nabla} \left(\frac{1}{\rho} \right) \wedge \vec{\nabla} p = -\frac{R}{M_r p} \vec{\nabla} T \wedge \vec{\nabla} p$. \vec{B} is zero when isothermal and pressure surfaces are parallel and, to first order of approximation in ϵ , \vec{B} becomes:

$$\vec{B} = -\frac{R}{M_r} \frac{\vec{\nabla} T \wedge \vec{\nabla} p}{p} = \frac{R}{M_r} \frac{\vec{\nabla} (p_h + \epsilon p_1) \wedge \vec{\nabla} T}{p_h + \epsilon p_1} = \epsilon \frac{R}{M_r} \left(\frac{\vec{\nabla} p_h \wedge \vec{\nabla} T'}{p_h} + \frac{\vec{\nabla} p_1 \wedge \vec{\nabla} T_h}{p_h} \right) + O(\epsilon^2).$$

Where $T(x, y, z) = T_h(z) + \epsilon T'(x, y, z) + O(\epsilon^2)$ has been used. Finally, noting that the velocity is of order ϵ , and that $\rho(x, y, z) = \rho_h(z) + \epsilon \rho'(x, y, z)$, one can rewrite the spatial derivatives in pressure coordinates defined as:

$$\frac{1}{\rho} \vec{\nabla} \rho v_i \partial y \equiv \left(\frac{\partial v_i}{\partial x} + \frac{\partial v_i}{\partial y} + \frac{\partial \omega_i}{\partial p_h} \right) + O(\epsilon^2) \equiv \vec{\nabla}_p v_i$$

with v_i being the components of the velocity vector and $\omega_i \equiv -g \rho v_i$. One can now use that $\vec{\nabla} p_h = -\rho_h g \vec{e}_r$ to write (A1) in pressure coordinates as:

$$\epsilon (2\vec{\Omega} \cdot \vec{\nabla}_p) \vec{v} = -\vec{B} + O(\epsilon^2) = -\epsilon \frac{R}{M_r} \left(-\rho_h g \frac{\vec{e}_r \wedge \vec{\nabla} T'}{p_h} + \frac{\vec{\nabla} p_1}{p_h} \wedge \vec{\nabla} T_h \right) + O(\epsilon^2). \quad (\text{A2})$$

The results (A1) and (A2) are the anelastic version of the thermal wind relations discussed for incompressible fluids by de Verdière and Schopp 1994 or Busse 1978. Expression (A2) shows that if pressure coordinates are used, the result for anelastic flows looks similar to incompressible flows under the notation change:

$$(p, -\frac{\partial}{\partial p} g \rho_h, \vec{\nabla}_p, \omega_3) \rightarrow (z, \frac{\partial}{\partial z}, \vec{\nabla}, w)$$

This analogy provides evidence in favor of a partial extension of results obtained in Oberbeck-Boussinesq models like discussed by Zhang and Schubert 1995 or references therein.

The component form of the thermal relation (A2) is:

$$\left\{ \begin{array}{l} \frac{\partial u}{\partial Z_p} \equiv \frac{1}{\rho} \frac{\partial \rho u}{\partial Z} = -\frac{R}{2\Omega M_r} \frac{1}{p_h} \left[\rho_h g \left(\frac{\partial T'}{\partial y} \right)_{p_h} + \left(\frac{\partial p_1}{\partial y} \right)_{p_h} \frac{\partial T_h}{\partial z} \right] + O(\epsilon^2) \\ \frac{\partial v}{\partial Z_p} \equiv \frac{1}{\rho} \frac{\partial \rho v}{\partial Z} = \frac{R}{2\Omega M_r} \frac{1}{p_h} \left[\rho_h g \left(\frac{\partial T'}{\partial x} \right)_{p_h} + \left(\frac{\partial p_1}{\partial x} \right)_{p_h} \frac{\partial T_h}{\partial z} \right] c + O(\epsilon^2) \\ \frac{\partial w}{\partial Z_p} \equiv \frac{1}{\rho g} \frac{\partial \rho_h g w}{\partial Z} \equiv -\frac{1}{\rho g} \frac{\partial \omega_3}{\partial Z} = O(\epsilon^2) \end{array} \right. \quad (\text{A3})$$

These three expressions are the 3D extension of the traditional geostrophic model. Following their conclusions as well as Veronis 1968 and Phillips 1968, this result will hold at *all* latitudes *at least* under the dynamical conditions where the traditional approach is valid. Some differences are apparent. The temperature gradient is the only effect appearing in the traditional 2D thermal wind relations. The reason for this is the inclusion of the baroclinic terms neglected in the permutation carried in section 5.3 of the lower order thermal wind relations. In the traditional approximation this problem does not appear. In our approach the density gradient is parallel to the vertical vector, which is not parallel to the variable along the axis of rotation Z_p . As a consequence, the vertical derivatives and the horizontal derivatives are strongly coupled. The new (non-traditional) terms that appear in our relations, arise from terms of order ϵ^1 neglected in the classical approach and the intermediate approach leading to expressions (4).

The thermal wind relations (A2) describe the change of the velocity field along the rotation axis. They are of interest for the sake of completeness and modeling purposes. However, their use in diagnostics is limited. They require independent simultaneous measurements of the temperature and pressure anomaly at levels much deeper than IR observations can reliably provide. This inconvenience was overcome by the intermediate approach leading to relations (4) in section 5.3.

Acknowledgements:

The authors wish to acknowledge the help and support of the staff of the NASA Infrared Telescope Facility for their support of the observations reported here, as well as Dr. Michael Ressler who set up MIRLIN initially in the run, and to Kartik Parija who assisted BMF and GSO in making the observations. The authors are grateful to two anonymous referees and to Dr. A. James Friedson for helpful discussions and careful reading of the manuscript. MTJ and BMF acknowledge support from NASA / National Research Council Associateships Program. GSO acknowledges support for this work from the Galileo mission and from research grants to the Jet Propulsion Laboratory, California Institute of Technology, from the NASA Planetary Astronomy and Planetary Atmospheres disciplines.

References:

- Atkinson, D.H., J.B. Pollack, A. Seiff, 1998: The Galileo Probe Doppler Wind Experiment: Measurements of the deep zonal winds on Jupiter. *J. Geophys. Res.*, **103**, 22911-22928.
- Banfield, D, P.J. Gierasch, S.W. Squyres, P.D. Nicholson, B.J. Conrath, K. Matthews 1996. 2 μ m Spectrophotometry of Jovian Stratospheric Aerosols-Scattering Opacities, Vertical Distributions, and Wind Speeds. *Icarus*, **121**, 380- 410.
- Brummel, N.H., N. E. Hurlburt, J. Toomre. 1996: Turbulent compressible convection with rotation. I flow structure and evolution, *The Astrophysical Journal* **473**, 494-513.
- Busse, F.H. 1976: A simple model of convection in the Jovian atmosphere, *Icarus*, **29**, 255-260.
- Busse, F.H. 1978: Thermal Convection in Rotating Systems. Proceedings of the 9th. U.S. Nat. Congr. of Appl. Mechanics. *ASME*, 299-305.
- Busse, F.H. 1983: A Model of Mean Zonal Flows in the Major Planets. *Geophys. Astrophys. Fluid Dynamics*, **23**, pp. 153-174.
- Chandrasekhar, S., 1961: *Hydrodynamic and Hydromagnetic Instability*, Clarendon Press, Oxford.
- Chahine, M. T., 1970: Inverse problems in radiative transfer: Determination of atmospheric parameters. *J. Atmos. Sci.* **27**, 960-967.
- Cho, J.Y-K., L. Polvani. 1996: The emergence of jets and vortices in freely evolving, shallow water turbulence on a sphere. *Phys. of Fluids* **8**, 1531-1552.
- Condie, S.A., P. B. Rhines. 1994: A convective model for the zonal jets in the atmospheres of Jupiter and Saturn. *Nature*, **367**, 711-713.
- Crisanti, A., Falcioni, M., Provenzale, A., Vulpiani, A. 1990: Passive advection of particles denser than the surrounding fluid. *Phys. Letters A* **150**, 79-84.

- Deming, D., M. J. Mumma, F. Espenak, D. Jennings, T. Kostiuk, G. Wiedemann, R. Loewenstein, J. Piscitelli, 1989: A search for p-Mode Oscillations of Jupiter: Serendipitous Observations of Nonacoustic Thermal Wave Structure. *Astrophys. J.* **343**, 456-467.
- Deming, D., D. Reuter, D. Jennings, G. Bjoraker, G. McCabe, K. Fast, G. Wiedemann, 1997: Observations and Analysis of Longitudinal Thermal Waves on Jupiter. *Icarus* **126**, 301-312.
- Dowling, T., A. P. Ingersoll 1989. Jupiter's Great Red Spot as a shallow water system. *J. Atmos. Sci.* **46**, 3256-3278.
- Dritschel, D.G., M. de la Torre Juárez, M.H.P. Ambaum, 1999. The Three-dimensional vortical nature of atmospheric and oceanic turbulent flows. *Phys. of Fluids* **11**, 1512-1520.
- D.G. Dritschel, M. de la Torre Juárez, 1996. The instability and breakdown of tall columnar vortices in a quasi-geostrophic fluid, *J. Fluid Mechanics*, **328**, 129-160.
- Gierasch, P.J., B. J. Conrath, J. A. Magalhães. 1986. Zonal mean properties of Jupiter's upper troposphere from Voyager infrared observations. *Icarus* **67**, 456-483, 1986.
- Gierasch, P.J., B. J. Conrath, 1993. Dynamics of the atmospheres of the outer planets - post-Voyager measurement objectives. *J. Geo. Res.* **98**, 5459-5469.
- Gill, A.E. 1982. *Atmosphere-Ocean Dynamics*, Academic Press Inc.
- Glatzmaier, G.A., P. H. Roberts. 1997. Simulating the geodynamo, *Contemporary Physics* **38**, 269-288.
- Holton, J.R. 1992: *An Introduction to Dynamic Meteorology*, 3rd ed. Academic Press Inc, San Diego.
- Holton, J.R., Haynes, P.H., McIntyre, M.E., Douglas, A.R., Rood, R.B., Pfister, L., 1995. Stratosphere-Troposphere exchange, *Reviews of Geophys.* **33**, 403-439.

- Hoskins, B.J., M.E. McIntyre and A.W. Robertson, 1985. On the use and significance of isentropic potential-vorticity maps, *Q.J.R. Meteorol. Soc.*, **111**, 877.
- Houghton, J.T. 1986: *The Physics of Atmospheres*, 2nd ed. Cambridge University Press.
- Hubbard, W.B. 1998. Gravitational Signature of Jupiter's Deep Zonal Flows. *Bull. Amer. Astron. Soc.* **30**.
- Ingersoll, A. P., G. Munch, G. Neugebauer and G. S. Orton, 1976. Results of infrared radiometer experiment on Pioneers 10 and 11. In Jupiter (T. Gehrels, ed.), Univ. of Arizona Press, Tucson, 197-205.
- Ingersoll, A.P., D. Pollard, 1982. Motion in the interiors and atmospheres of Jupiter and Saturn: Scale analysis, anelastic equations, barotropic stability criterion. *Icarus* **52**, 62-80.
- Ingersoll, A.P., C.C. Porco, 1978. Solar heating and Internal Heat flow on Jupiter. *Icarus* **35**, 27-43.
- Limalye, S., 1986. Jupiter: New estimates of the mean zonal flow at the cloud level. *Icarus* **65**, 335-352.
- Lindal, G.F., G. E. Wood, G. S. Levy, J. D. Anderson, D. N. Sweetnam, H. B. Holtz, B. J. Buckles, D. P. Holmes, P. E. Doms, V. R. Eshleman, G. L. Tyler, T. A. Croft. 1981. The atmosphere of Jupiter: An analysis of the Voyager radio occultation measurements. *J. Geophys. Res.* **86**, 8721-8727.
- Magalhães, J. A., A. L. Weir, P. J. Gierasch, B. J. Conrath, S. S. Leroy. 1989. *Nature* **337**, 444-447.
- Magalhães, J.A., A. L. Weir, B. J. Conrath, P. J. Gierasch, and S. S. Leroy. 1990. Zonal motion and structure in Jupiter's upper troposphere from Voyager infrared and imaging observations. *Icarus* **88**, 39-72.
- Miles, J.W. 1974. On Laplace's tidal equations. *J. Fluid Mech.* **66**, 241-260.

- Orton, G.S., J. F. Appleby, J. V. Martonchik. 1982. The effect of ammonia ice clouds in the atmosphere of Jupiter on outgoing thermal radiation. *Icarus* **52**, 94-116.
- Orton, G.S., A. J. Friedson, P. A. Yanamandra-Fisher, J. Caldwell, H. B. Hammel, K. H. Baines, J. T. Bergstralh, T. Z. Martin, R. A. West, G. J. Veeder Jr., D. K. Lynch, R. Russel, M. E. Malcolm, W. F. Golisch, D. M. Griep, C. D. Kaminski, A. T. Tokunaga, T. Herbst, M. Shure. 1994. Spatial organization and time Dependence of Jupiter's tropospheric temperatures, 1980-1993. *Science* **265**, 625-631.
- G. S. Orton, B. M. Fisher, S. T. Stewart, A. J. Friedson, J. L. Ortiz, M. Marinova, W. Hoffmann, J. Hora, M. Ressler, S. Hinkley, V. Krishnan, M. Masanovic, J. Tesic, A. Tziolas, and K. Parija. 1998. The Galileo Probe entry site: Characteristics of the Galileo Probe entry site from earth-based remote sensing observations. *J. Geophys. Res.* **103**, 22791-22814
- Pedlosky, J., 1987. *Geophysical Fluid Dynamics*, 2nd ed. Springer Verlag. New York.
- Phillips, N.A., 1966. The equations of motion for a shallow rotating atmosphere and the "traditional approximation". *J. Atmos. Sci.* **23**, 626-628.
- Phillips, N. A., 1968. Reply. *J. Atmos. Sci.* **25**, 1155-1157.
- Pirraglia, J.A., B. J. Conrath, M. D. Allison, P. J. Gierasch. 1981. Thermal structure and dynamics of Saturn and Jupiter. *Nature* **292**, 677-679.
- Ressler, M. E., M. W. Werner, J. Van Cleve, J., and H. A. Chou. The JPL Deep-Well Mid-Infrared Array Camera. 1994. In *Infrared Astronomy with Arrays: The Next Generation*, Ed. Ian McLean, *Experimental Astronomy* **3**, 277.
- Rhines, P. B. 1975. Waves and turbulence on a beta plane. *J. of Fluid Mech.*, **69**, 417-433.
- Seiff, A., D. B. Kirk, T. C. D. Knight, R.E. Young, J. D. Mihalov, L. A. Young, F.

- S. Milos, G. Schubert, R. C. Blanchard, D. Atkinson. 1998. Thermal structure of Jupiter's atmosphere near the edge of a 5-micron hot spot in the North Equatorial Belt. *J. Geophys. Res.* **103**, 22857 - 22890.
- Showman, A., A. P. Ingersoll. 1998. Interpretation of Galileo probe data and implications for Jupiter dry downdrafts. *Icarus* **132**, 205-220.
 - Tritton, J., 1977. *Physical Fluid Dynamics*, 1st ed. Van Nostand Reinhold. U.K.
 - Vasavada A. R., and 13 colleagues, 1998. Galileo imaging of Jupiter's atmosphere: the Great Red Spot, equatorial region, and White Ovals. *Icarus* **135**, 251-264.
 - de Verdière, A. C., R. Schopp. 1994. Flows in a rotating spherical shell: The equatorial case. *J. Fluid Mech.* **276**, 233-260.
 - Veronis, G., 1968. Comments on Phillips' Proposed simplification of the equations of motion for a shallow rotating atmosphere. *J. Atmos. Sci.* **25**, 1154-1155.
 - Yano, J-I., 1994. A critical review on the dynamics of Jovian atmospheres. *Chaos* **4**, 287-297.
 - White, A.A., R.A. Bromley, 1995. Dynamically consistent, quasi-hydrostatic equations for global models with a complete representation of the Coriolis force. *Q. J. R. Meteorol. Soc.* **121**, 399-418.
 - Williams, G.P. 1996. Jovian Dynamics. Part I: Vortex stability, structure and genesis. *J. Atmos. Sci.* **53**, 2685-2734.
 - Williams, G.P., Robinson, J.B., 1973. Dynamics of a convectively unstable atmosphere: Jupiter ? *J. Atmos. Sci.* **30**, 684-717.
 - Zhang, K., G. Schubert. 1995. Spatial symmetry breaking in rapidly rotating convective spherical shells. *Geophys. Res. Lett.* **22**, 1265-1268.
 - Zhang, K., G. Schubert. 1996. Penetrative convection and zonal flow on Jupiter. *Science* **273**, 941-943.

Tables

Table I

	$U \sim V \sim c/2 \text{ (m s}^{-1}\text{)}$	$W \text{ (m s}^{-1}\text{)}$	$\Delta x \sim \Delta y \text{ (km)}$	$\Delta z \text{ (km)}$	$\Omega \text{ (s}^{-1}\text{)}$
	$\lesssim 300$	$\lesssim 2$	~ 4700	~ 25	$1.76 \cdot 10^{-4}$
	Advection $(\vec{v} \cdot \vec{\nabla})\vec{v}$		Cyclostrophy (\vec{v}^2/r)	Coriolis $(2\Omega \vec{v})$	Gravity
U, V	$\lesssim 3 \cdot 10^{-2} \text{ ms}^{-2}$		$\lesssim 10^{-3} \text{ ms}^{-2}$	$\lesssim 10^{-1} \text{ ms}^{-2}$	23 ms^{-2}
W	$\lesssim 3 \cdot 10^{-4} \text{ ms}^{-2}$		$\lesssim 10^{-3} \text{ ms}^{-2}$	$\lesssim 10^{-1} \text{ ms}^{-2}$	23 ms^{-2}
	Advection $(\vec{u} \cdot \vec{\nabla})T$		Diffussion $k\nabla^2 T$	Heat sources $(T_e - T)/\tau_r$	
T	$\lesssim 10^{-4}$		$\lesssim 10^{-13}$	$\lesssim 3 \cdot 10^{-8}$	

Figure Captions

Figure 1. Normalized weighting functions for each observational bandpass. The normalized weighting functions show the relative contribution to the outgoing flux from each pressure level.

Figure 2. Composite global temperature maps as a function of planetocentric latitude and west System III longitude. Note the the bright feature near 25° W, 25° N, is the Jovian moon Io which was transiting during the observation.

Figure 3. Mean zonal temperatures for our four pressure levels as a function of planetographic latitude. The error bars represent the one standard deviation level of all of the available data at each latitude. The longitudes containing the Io image were excluded.

Figure 4. Normalized density anomalies for the four pressure levels. Note the the dark feature near 25° W, 25° N, is the Jovian moon Io which was transiting during the observation.

Figure 5. Mean zonal values of the zonal component of the geostrophic wind shear, $\partial u_g / \partial z^*$, for the upper and lower pressure levels, compared to the cloud derived winds (solid line) from Limaye 1986. Results using the classical hydrostatic approximation are shown as filled circles. Results using equation (2) are shown as open squares. The upper two panels are scaled to show the full range. The lower panels are scaled to show the details of the small amplitude structure. Panel (a) corresponds to the 100 mbar pressure level, (b) to 400 mbar, (c) to 100 mbar, and (d) to 400 mbar.

Figure 6. The zonal component of the geostrophic wind shear, $\partial u_g / \partial z^*$, for each pressure level. The Jovian moon Io transiting Jupiter causes an artifact near 25° W, 25° N.

Figure 7. The meridional component of the geostrophic wind shear, $\partial v_g / \partial z^*$, for each pressure level. The Jovian moon Io transiting Jupiter causes an artifact near 25° W, 25° N.

Figure 8. The vertical component of the geostrophic wind shear, $\partial w_g / \partial z^*$, for each pressure level. The Jovian moon Io transiting Jupiter causes an artifact near 25° W, 25° N.

Figure 9. Mean zonal averages of the vertical transport in units of $w\tau_r/H$, for the four pressure levels. Panel (a) corresponds to the 100 mbar pressure level, (b) to 200 mbar, (c) to 316 mbar, and (d) to 400 mbar.

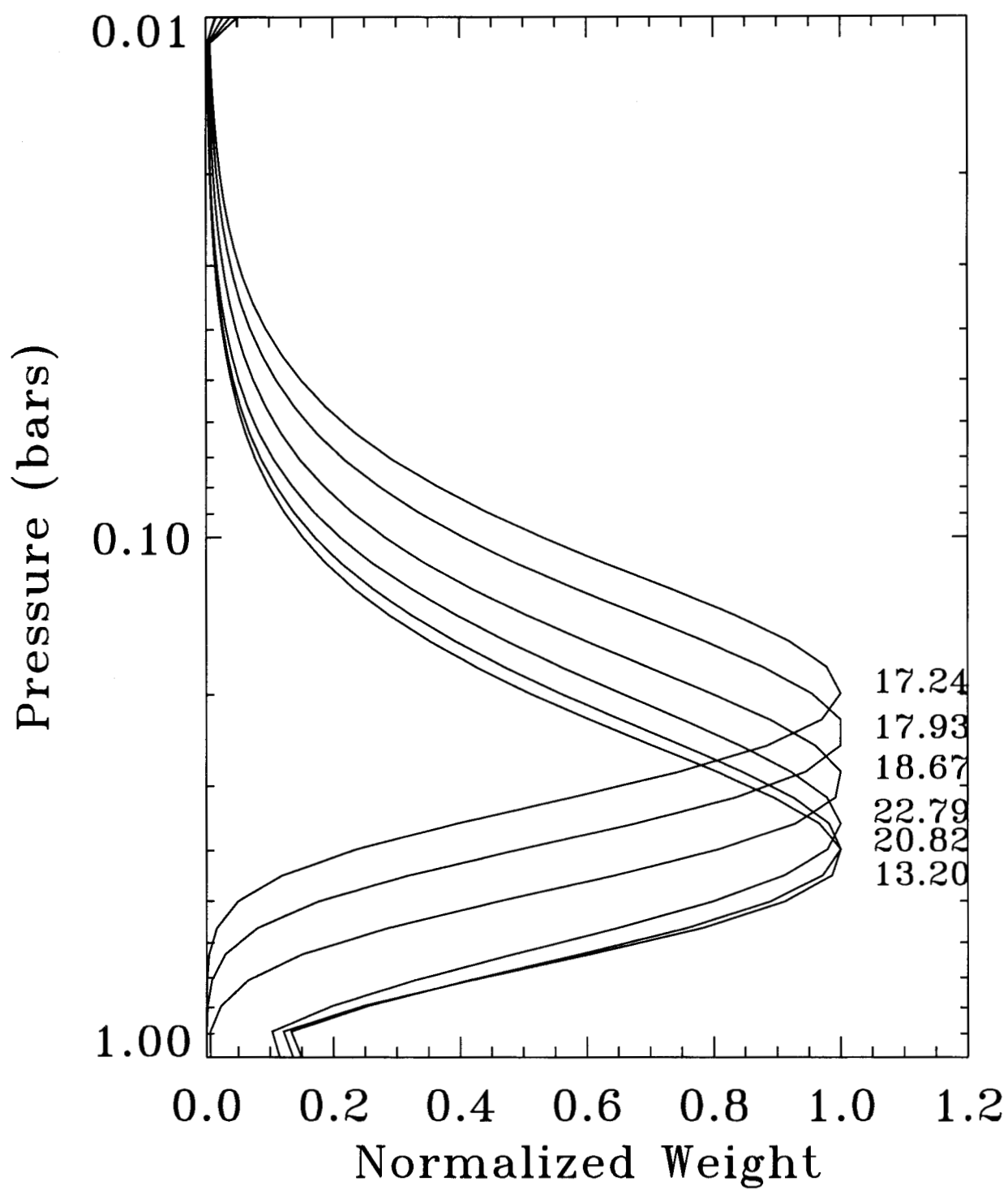
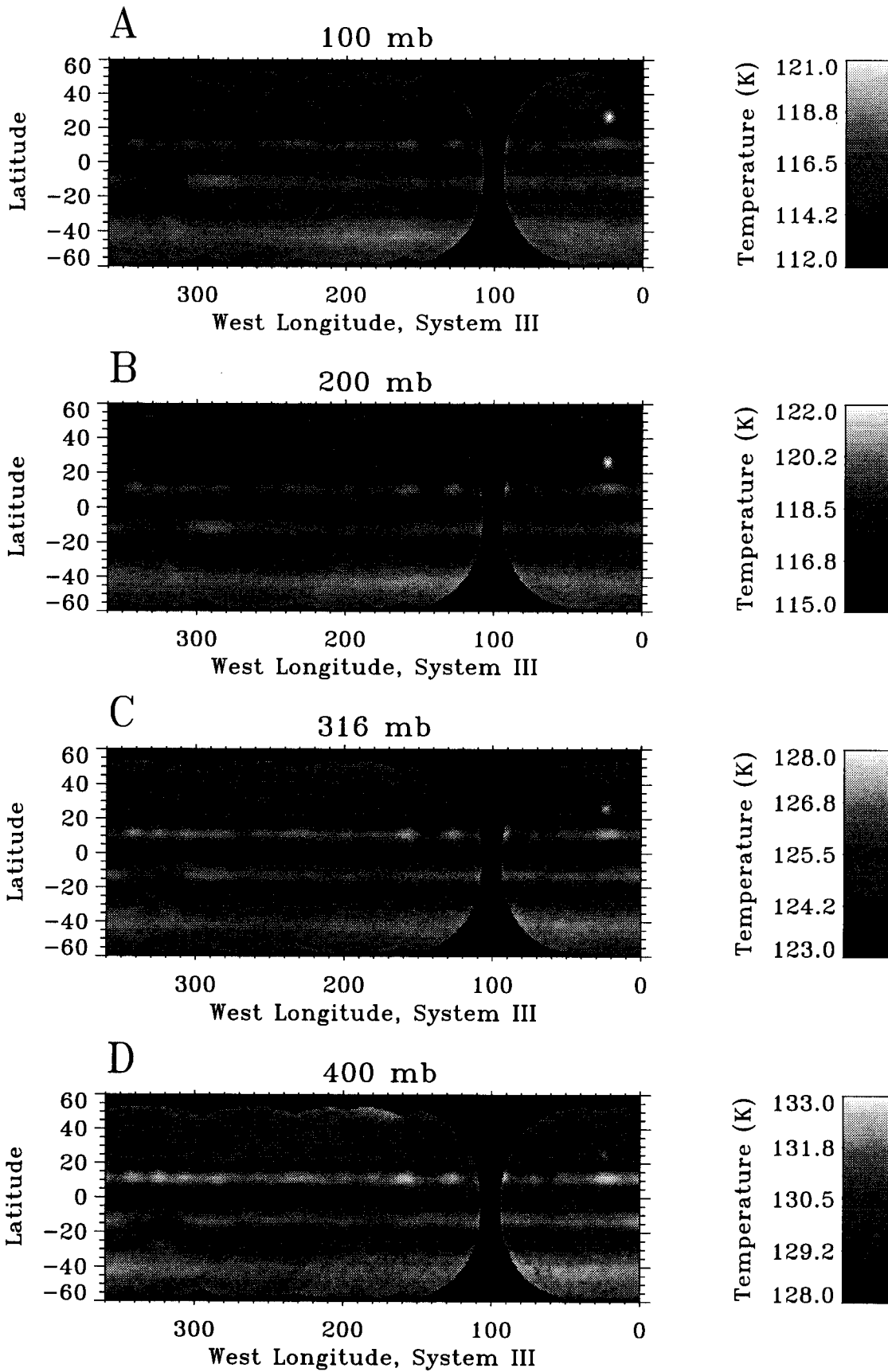


Figure 1



Figures 2 a-d

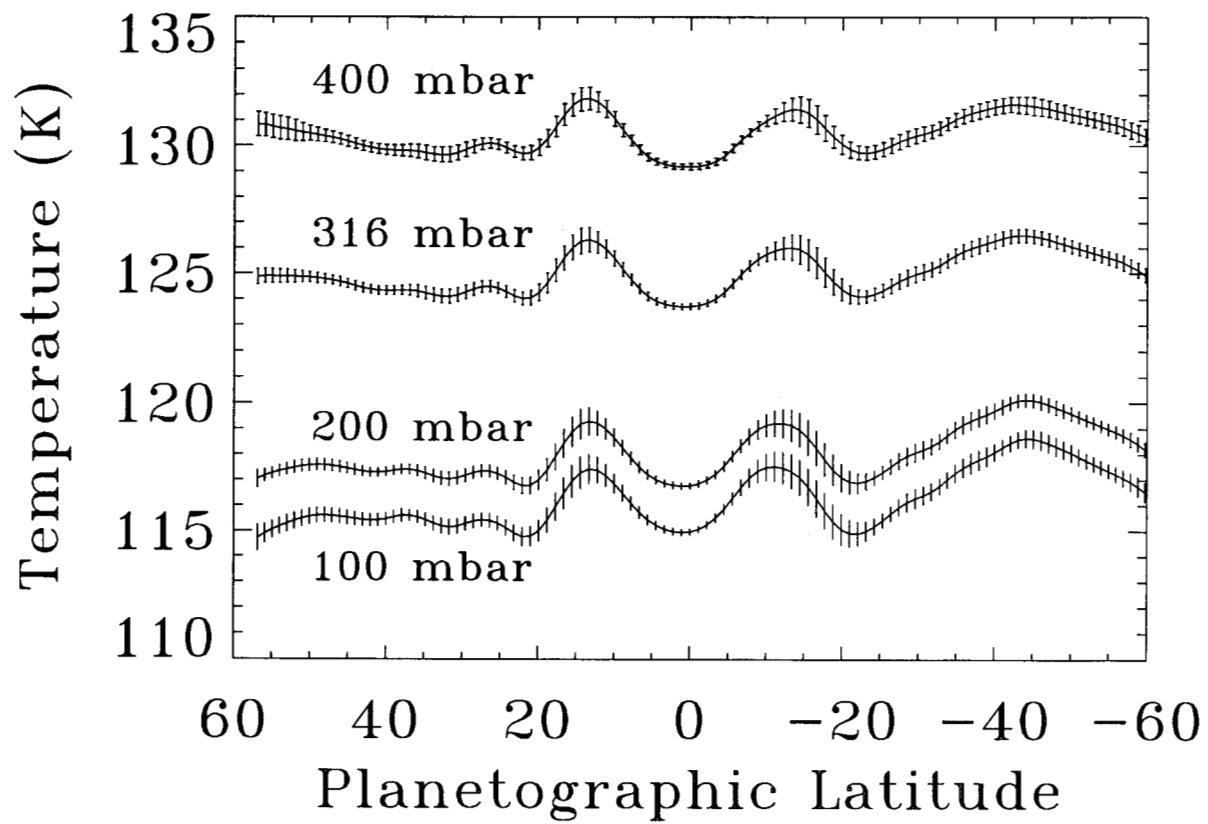
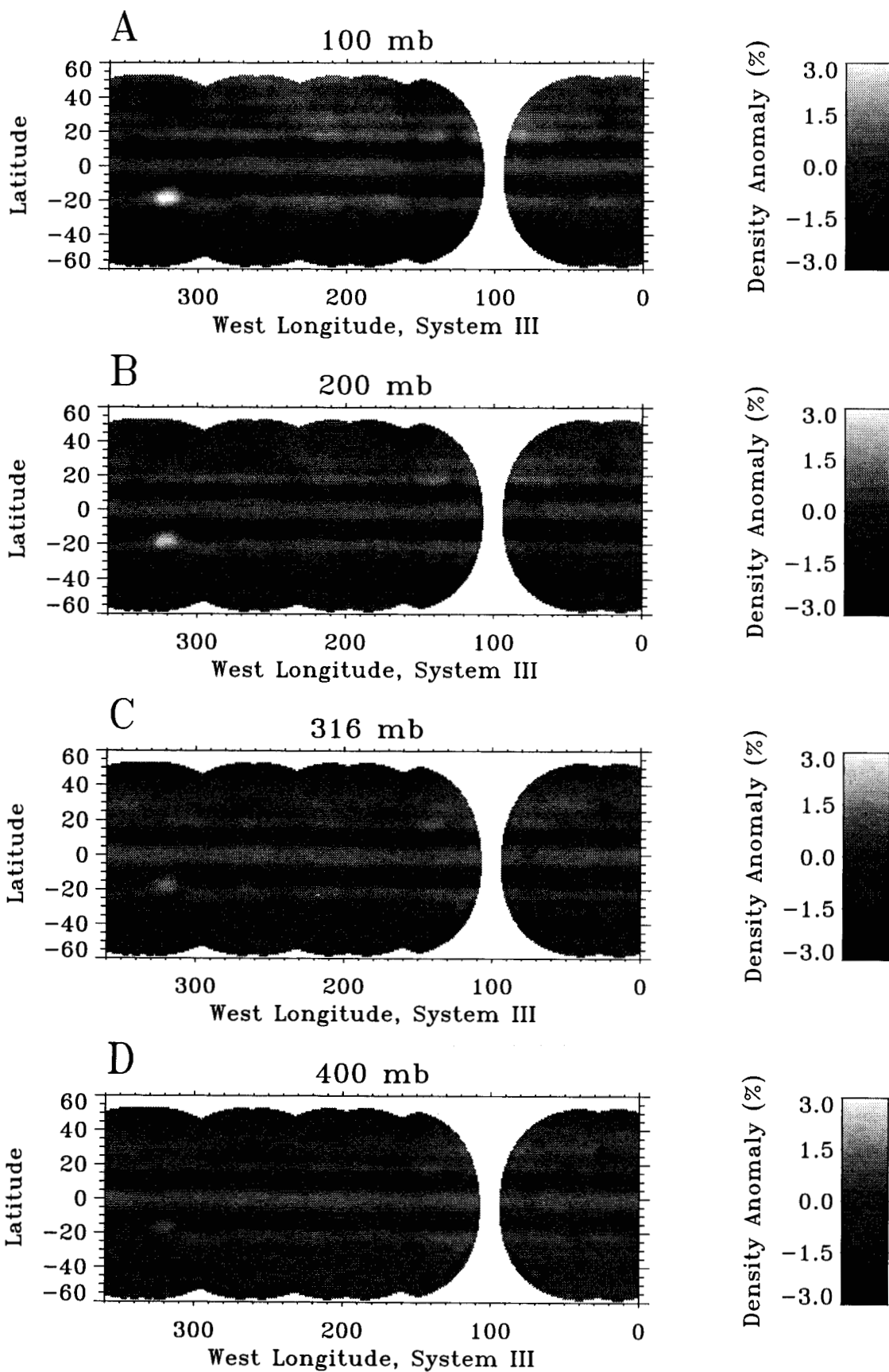


Figure 3



Figures 4 a-d

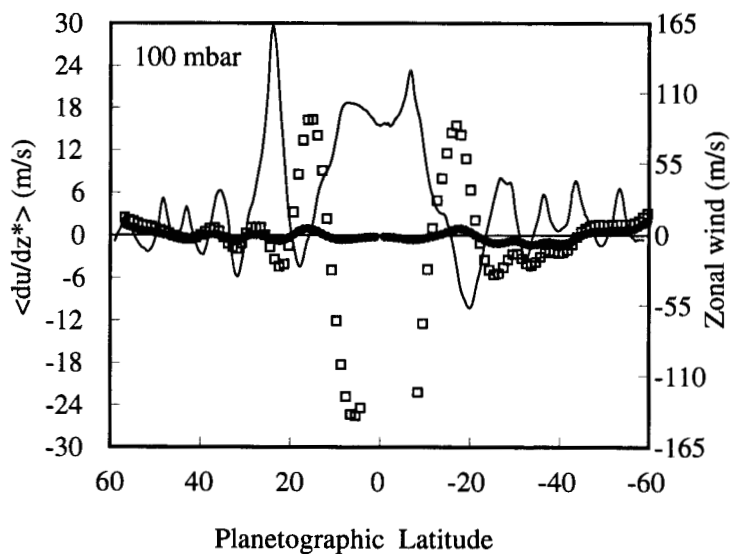


Figure 5a

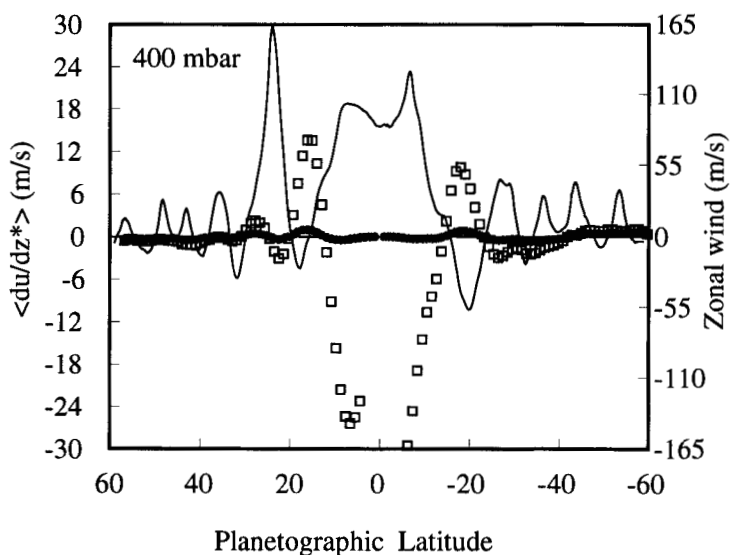


Figure 5b

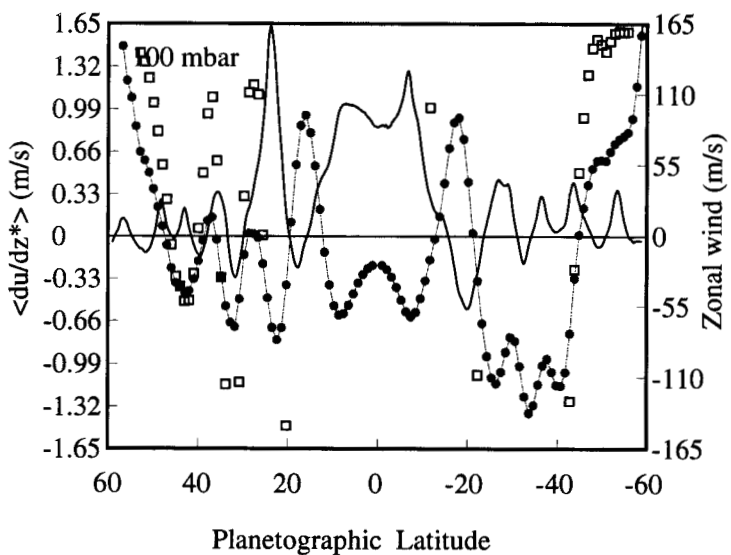


Figure 5c

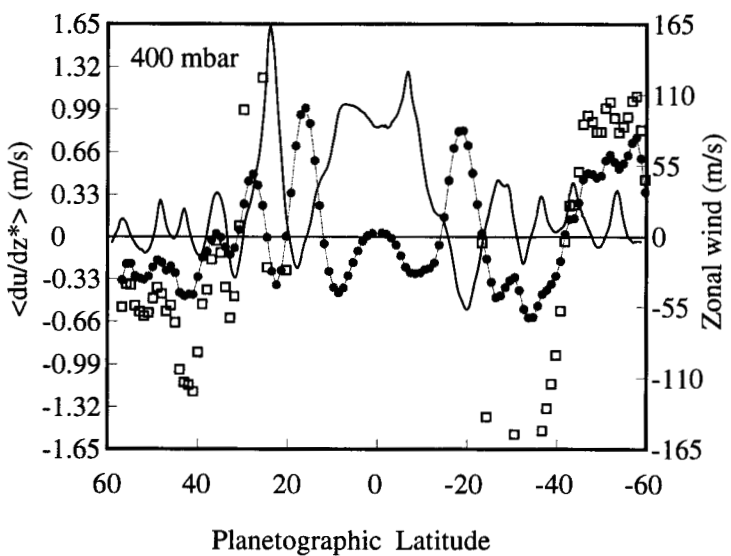
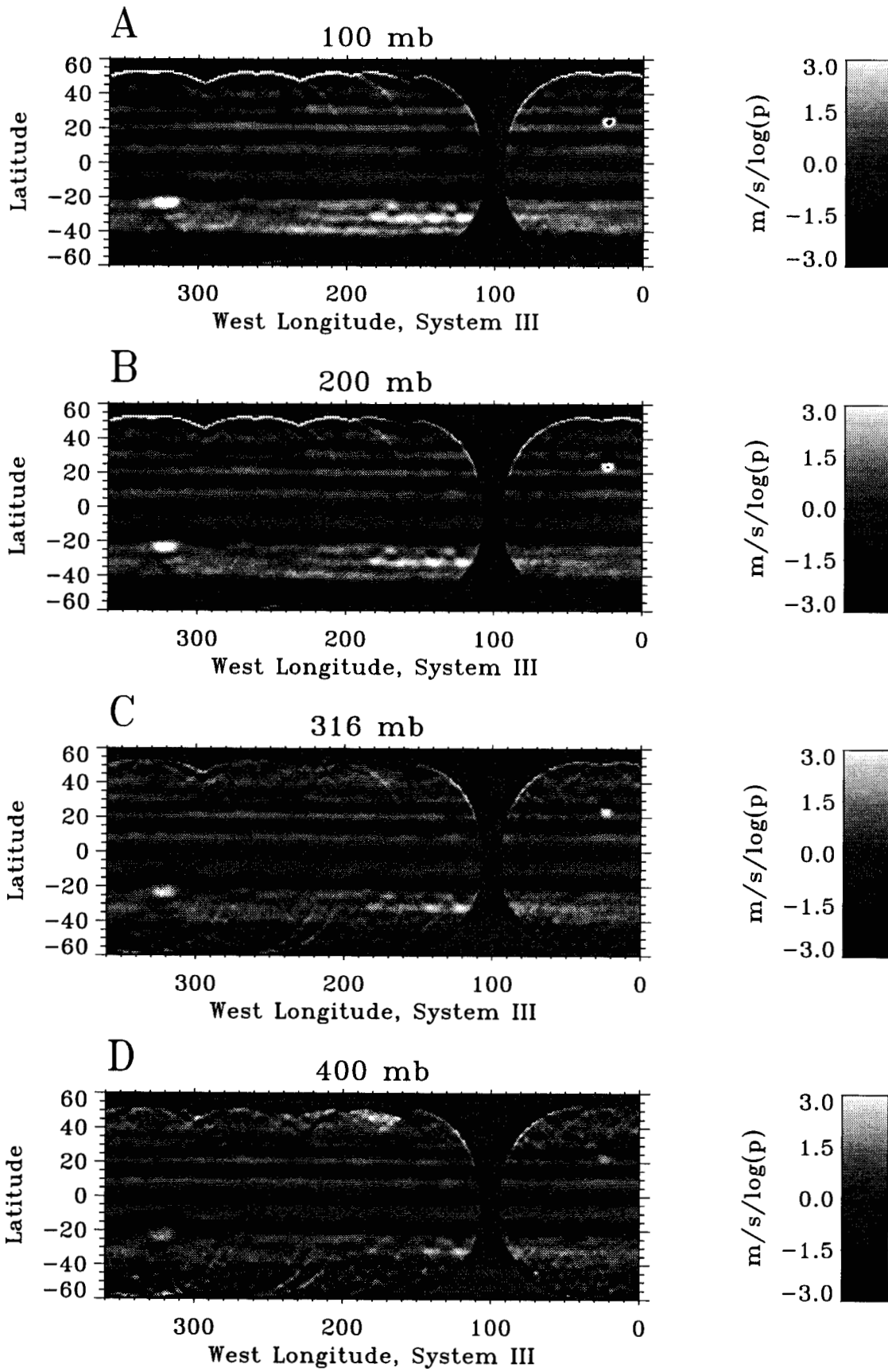
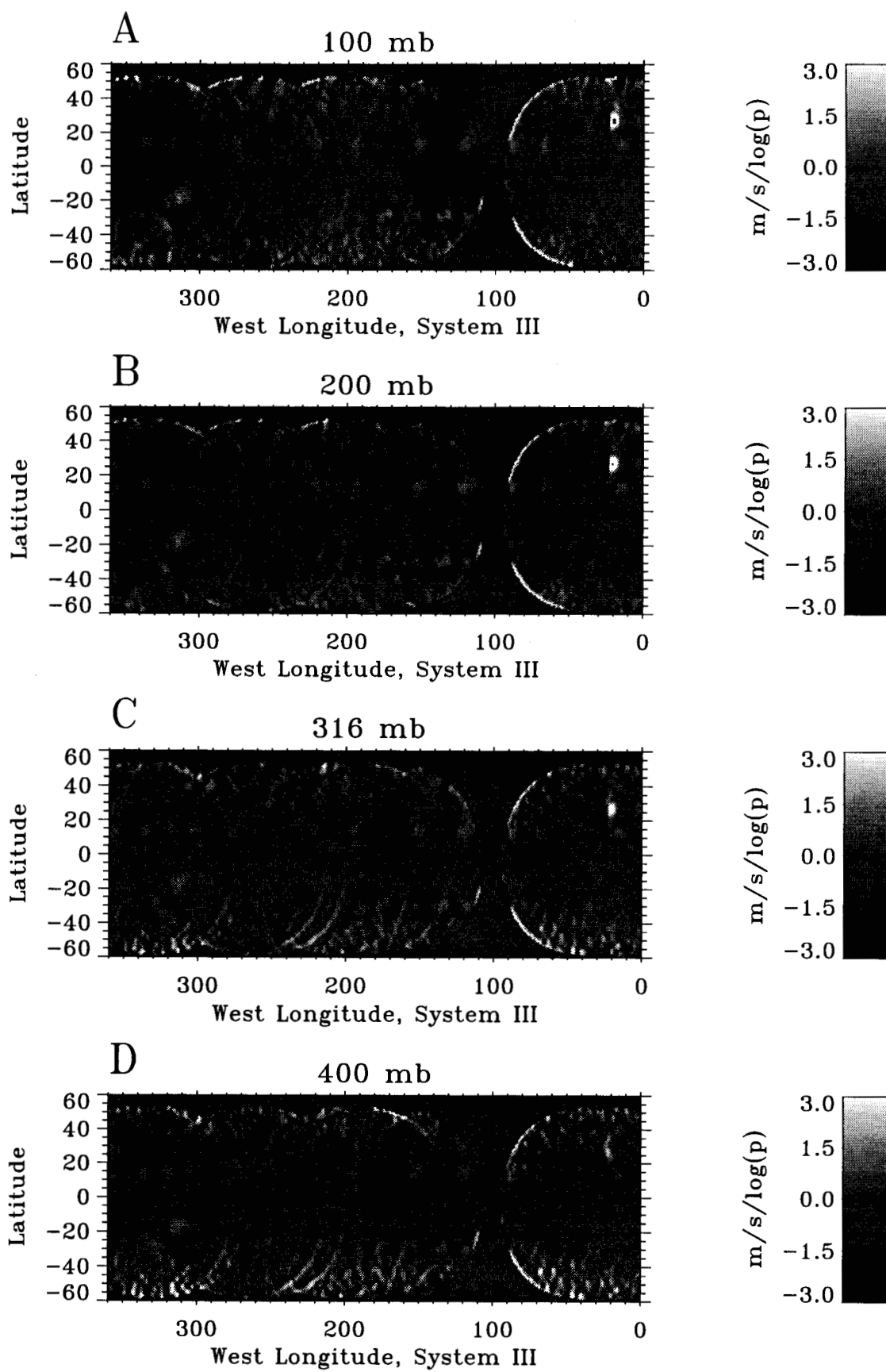


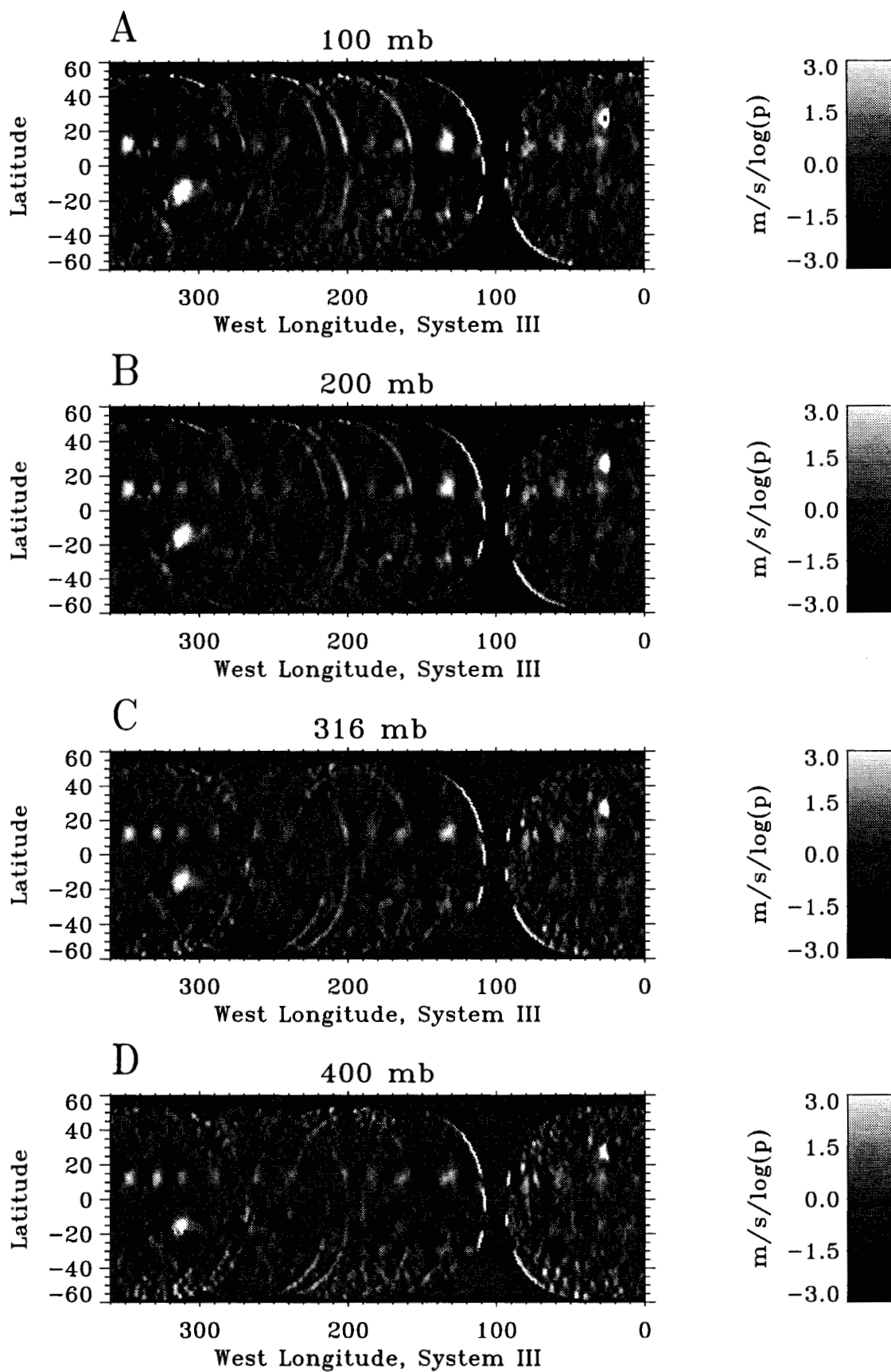
Figure 5d



Figures 6 a-d



Figures 7 a-d



Figures 8 a-d

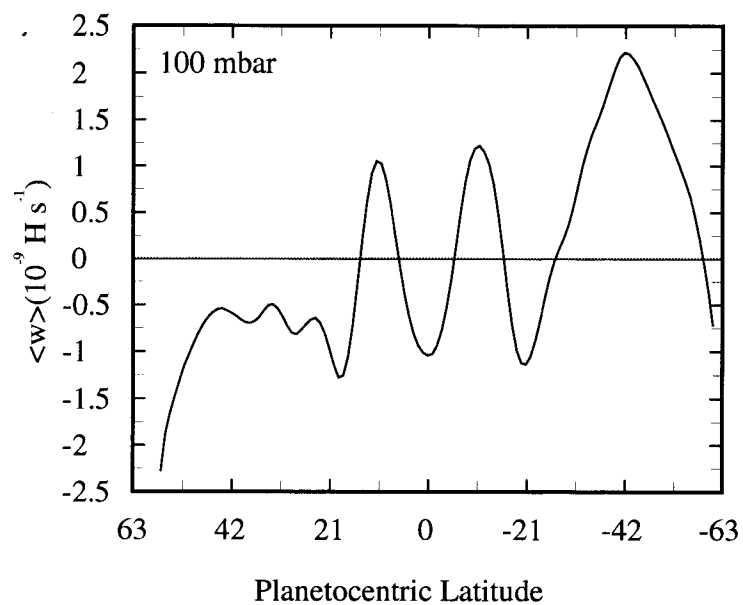


Figure 9a

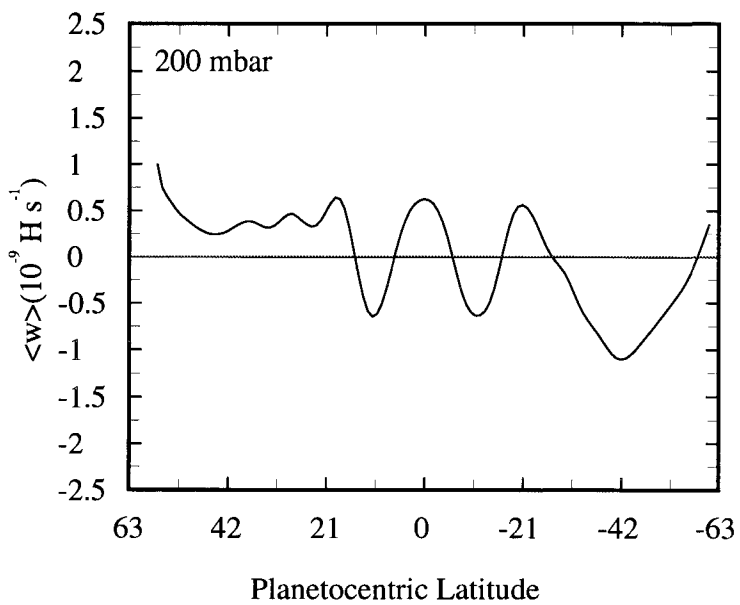


Figure 9b

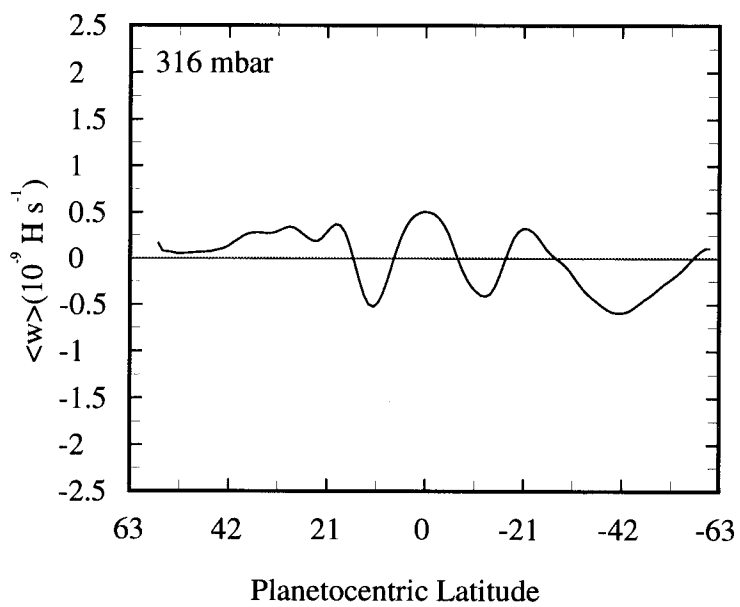


Figure 9c

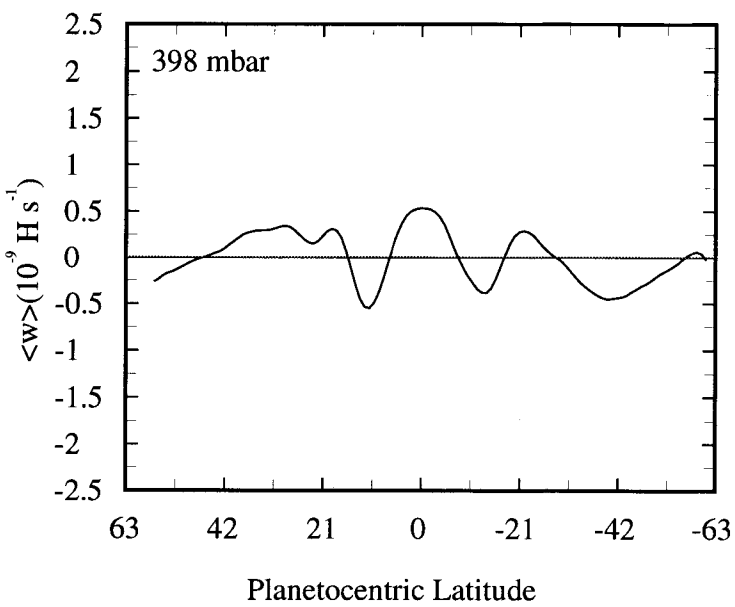


Figure 9d